Microseismicity and permeability enhancement of hydrogeologic structures during massive fluid injections into granite at 3 km depth at the Soultz HDR site

K. F. Evans,[1] H. Moriya,[2] H. Niitsuma,[2] R. H. Jones,[3] W. S. Phillips,[4] A. Genter,[5] J. Sausse,[6] R. Jung[7] and R. Baria[8]

[1]*Geology Institute, Swiss Federal Institute of Technology, Zürich, Switzerland. E-mail: keith.evans@erdw.ethz.ch*
[2]*Graduate School of Environmental Studies, Tohoku University, Sendai, Japan*
[3]*Vetco Gray, Rosemanowes, Penryn, Cornwall, UK*
[4]*Seismic Research Center, Los Alamos National Laboratory, New Mexico, USA*
[5]*BRGM, Orleans, France*
[6]*UMR CNRS 7566 G2R, University of Nancy, Vandoeuvre, France*
[7]*BGR, Hannover, Germany*
[8]*GEIE, Route de Kutzenhausen, Soultz-sous-Forêts, France*

SUMMARY

A high-rate injection of 20 000 m^3 of water into granite between 2.8 and 3.4 km depth at the Soultz hot dry rock (HDR) test site in France in 1993 September led to a 200-fold increase in borehole transmissivity and produced a subvertical cloud of microseismicity of dimensions 0.5 km wide, 1.2 km long, 1.5 km high and oriented 25°NW. The resulting data set is unusually complete and well suited to studying permeability creation/enhancement processes in crystalline rock and the utility of microseismic data for revealing them. Although the microseismic cloud defined using joint hypocentre determination (JHD) locations was diffuse and showed little structure, application of the collapsing method showed it to be composed largely of discrete tubes and planes that propagated coherently. One prominent structure that extended 350 m downwards from the vicinity of a flow inlet early in the injection and that appears to contain a major flow path was subjected to detailed investigation to establish its hydrogeologic nature and the mechanisms underpinning its inferred permeability enhancement. High-resolution microseismic mapping techniques (i.e. multiplets and clustering) showed it to be a subvertical, NNW–SSE striking, fracture zone of width 10–20 m. The strike and scale of the structure identifies it as a member of a family of hydrothermally altered, cataclastic shear structures that constitute the primary permeable paths for fluid migration within the rock mass, both under ambient and forced fluid flow conditions. The microseismicity occurred on subvertical, small-scale fractures within the cataclastic shear zone whose azimuths scatter within 22° of parallel to the parent structure. Although the structure is likely to have been naturally permeable to some degree, its permeability appears to have been significantly enhanced as a consequence of the injection. The most likely mechanism of permeability enhancement, which is in accord with the strong preference for the microseismicity to grow downwards, involves strike-slip shearing, which produced the opening of vertical tubes at along-strike jogs in the fault (the so-called Hill mesh). Seismic moment release averaged over the structure suggests shear displacements of at least 0.3 mm occurred, which are sufficient to generate aperture changes that are hydraulically significant. The preponderance of discrete structures within the microseismic cloud after collapsing suggests that significant flow and permeability enhancement (i.e. stimulation) within the rock mass is largely confined to the interiors of shear zones that appear to have a spacing of approximately 100 m.

Key words: enhanced geothermal systems, fluids and rocks, hot dry rock, induced microseismicity, permeability creation.

1 INTRODUCTION

Hot dry rock (HDR) systems offer the attractive prospect of producing large quantities of CO_2-emission-free energy from deep, low-porosity, crystalline rocks that can be found at drillable depths in many parts of the world. The HDR concept is to drill two or more boreholes to depths where temperatures are of commercial interest and extract the heat from the rock mass between them by circulating fluid around the loop. The natural permeability of deep, crystalline rocks is generally too low to permit the requisite flow to pass between the holes and thus must be enhanced. This is accomplished by an operation referred to as reservoir stimulation (or sometimes as hydrofracturing) in which a large volume of fluid is injected into the rock mass at high flow rates. The specific objective is to raise the pore pressure within the target reservoir volume, thereby promoting the failure and dilation of natural fractures and resulting in a network of connected, permeable fractures. The ability to design the reservoir stimulation process to suit different geological situations is crucial to the establishment of HDR systems as a commercially viable technology and this lends great importance to understanding of the processes through which flow channels are created and their permeability increased. The early notion that the high-pressure injections would serve to drive extensive mode I hydrofractures through the crystalline rock, as is done routinely in hydrofracture treatments of oil and gas reservoirs, is not supported by the experience at the seven HDR tests facilities conducted to date (see Evans *et al.* 1992; Jupe *et al.* 1993; Abé *et al.* 1999, for summaries). Rather, it appears that shearing of fractures and faults within the rock mass is the primary permeability creating mechanism, although the essential details of the processes, such as the scale and magnitude of shearing surfaces and the geometry of the openings and potential flow paths that result, remain uncertain. This poor state of knowledge reflects the difficulty of obtaining information about changes in the rock mass remote from the boreholes.

The most promising approach to the problem of determining the location of connected flow paths within the rock mass is to monitor the microseismicity that invariably accompanies the injections. The focal mechanisms of the individual events where they have been obtained are usually found to be predominantly double couple, reflecting localized, planar shear failure (Cash *et al.* 1983; Cornet & Julian 1989; Jost *et al.* 1998; Tezuka & Niitsuma 2000). At deep sites, it is usually necessary to install a network of seismic sensors in deep boreholes to secure adequate sensitivity to small magnitude events. Given the cost of drilling such boreholes, the downhole networks are invariably sparse, which deleteriously impacts the ability to obtain fault plane solutions and, most importantly, precise locations. The location errors obtained by applying standard methods such as joint hypocentre determination (JHD; Frohlich 1979) to analysts' picks of phase arrivals are usually sufficiently large as to produce a cloud-like image of the locations showing little structure. Significant advances have been made in the past few years in the ability to resolve geometrically significant structures within such clouds (Niitsuma *et al.* 1999; Thurber & Rabinowitz 2000; Fehler *et al.* 2001). In HDR reservoirs, the structures are typically found to be tubes or planes (Roff *et al.* 1996) and have sizes that are much larger than the source dimensions of the individual events (Gaucher 1998). However, basic questions remain as to how to interpret the microseismic structures in terms of fluid flow within the rock mass. Neglecting poro-elastic phenomena (e.g. Maillot *et al.* 1999), the occurrence of microseismicity at a point remote from the injection interval indicates that the point has a hydraulic connection to the borehole interval. It does not necessarily mean that significant hy-

draulic flow occurs along the connection (Cornet & Scotti 1993). Indeed, it is generally very difficult to establish that a seismic structure highlights a hydrologically significant (i.e. flowing) structure (Baisch *et al.* 2002). Examples have been reported at the Fjällbacka HDR test site in Sweden (Wallroth *et al.* 1996) and the Hiijiori site in Japan (Tezuka & Niitsuma 2000).

In this paper, we use an exceptionally rich, diverse data set to investigate the nature of microseismicity occurring during a massive fluid injection into the previously undisturbed granite basement at 3–3.5 km depth at the European HDR project site at Soultz-sous-Forêts in France. Application of the collapsing method of image enhancement to the microseismic cloud revealed it was composed largely of discrete structures that were lines or planes. One such structure that extends 300 m downwards from a flow zone in the borehole was subjected to intensive study. Evidence suggests this structure supported significant flow following the injections and was thus stimulated. We use high-resolution microseismic imaging, borehole geophysical logging, geological and hydraulic data to identify its hydrogeologic nature, understand the character of the microseismicity and constrain the stimulation mechanisms.

2 SITE DESCRIPTION

The European Communities HDR test site is located near Soultz-sous-Forêts in the Rhine graben some 40 km north of Strasbourg, France (Fig. 1). At the site, the block-faulted, Hercynian-age, monzogranite basement lies at a depth of 1.4 km below a cover of Permian, Mesozoic and Cenozoic sediments. In 1992, well GPK1, which was originally drilled to 2000 m, was extended to 3600 m and the casing shoe set at 2850 m leaving 750 m of $6-\frac{1}{4}$ inch open hole. The bottom hole temperature was 160 °C. A plan view of the site as it existed in 1993 is shown in Fig. 2. Four other holes in addition to GPK1 existed at that time. Borehole EPS1 was drilled and fully cored to 2227 m in 1991, thereby providing detailed information about the nature and history of the granite and its natural fractures (Genter & Traineau 1992). The other three wells, 4550, 4601 and 4616, are old oil industry holes that were extended to reach a few tens of metres into the basement and four-component accelerometers placed at their bottoms for microseismic monitoring. The site has since been developed further. In 1995, a second borehole was drilled to 3.8 km and linked to GPK1 through stimulation injections to form a circulation loop at 3 km (Baumgärtner *et al.* 1996, 1998). More recently, the 3.8 km hole was extended to 5 km and a further two holes drilled to 5 km with a view to developing a deeper circulation system (Weidler *et al.* 2002; Hettkamp *et al.* 2004). However, in this paper, we will focus exclusively on the effect on the rock mass of the major injections conducted on GPK1 in 1993.

3 CHARACTERIZATION OF THE NATURAL STATE OF THE GRANITE ROCK MASS

3.1 Natural fracture characteristics

Following the completion of well GPK1, a suite of geophysical logs were run that included several fracture imaging logs. Fig. 3 shows the distribution along the hole of some 500 fractures identified on images from a Schlumberger Ultrasonic Borehole Imager (UBI) log (Evans 2000). Although these represent only the widest 25 per cent of fractures having acoustic apertures greater than approximately 1–2 mm (Genter *et al.* 1997),
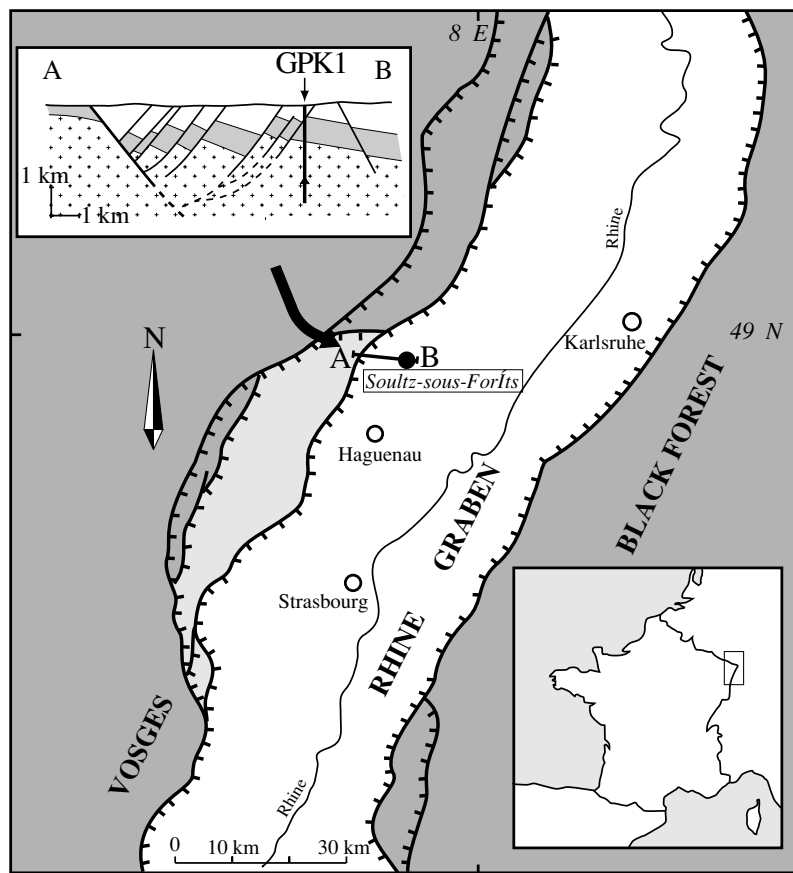
Figure 1. Location of the Soultz hot dry rock (HDR) test site near the centre of the Upper Rhine graben. The 3.6-km-deep borehole GPK1 penetrates a basement horst structure at a depth of approximately 1400 m. Vertical section A–B: cross-pattern is granite (dark grey in plan), light grey denotes Mesozoic sediments and white indicates Oligocene and Miocene sediments. Modified after Dezayes *et al.* (1995).
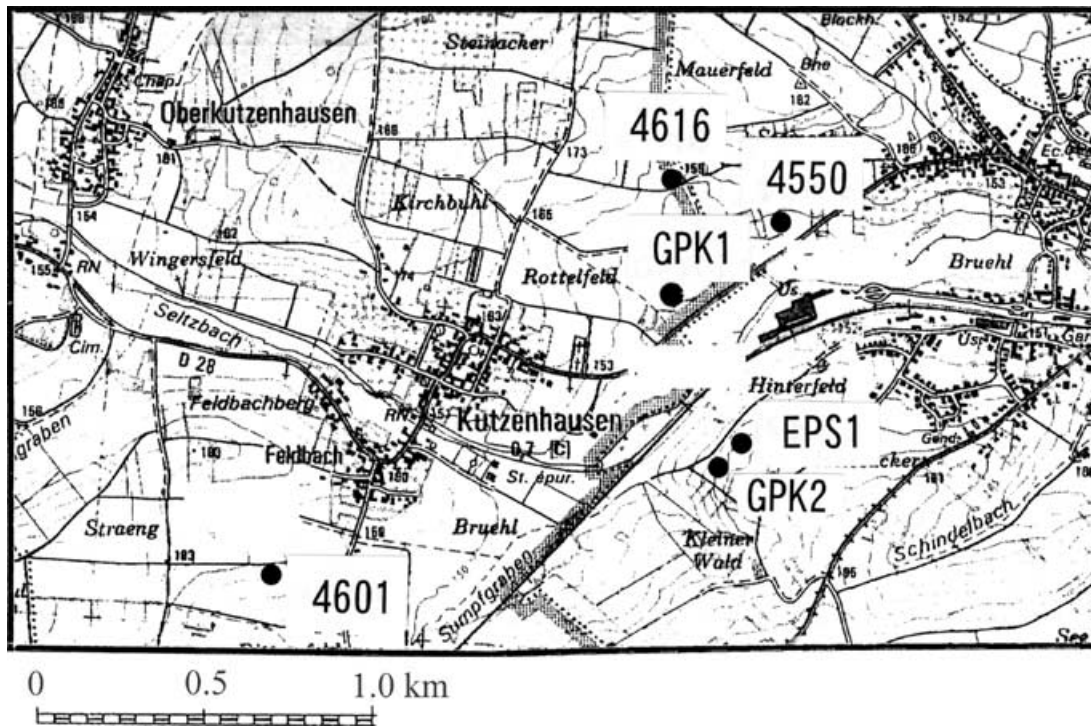

Figure 2. Plan view of the test site as it existed in 1993 showing the location of well heads. The numbered wells are seismic observation wells extending into the top of the granite. EPS1 is a hole that was continuously cored to 2.2 km depth.
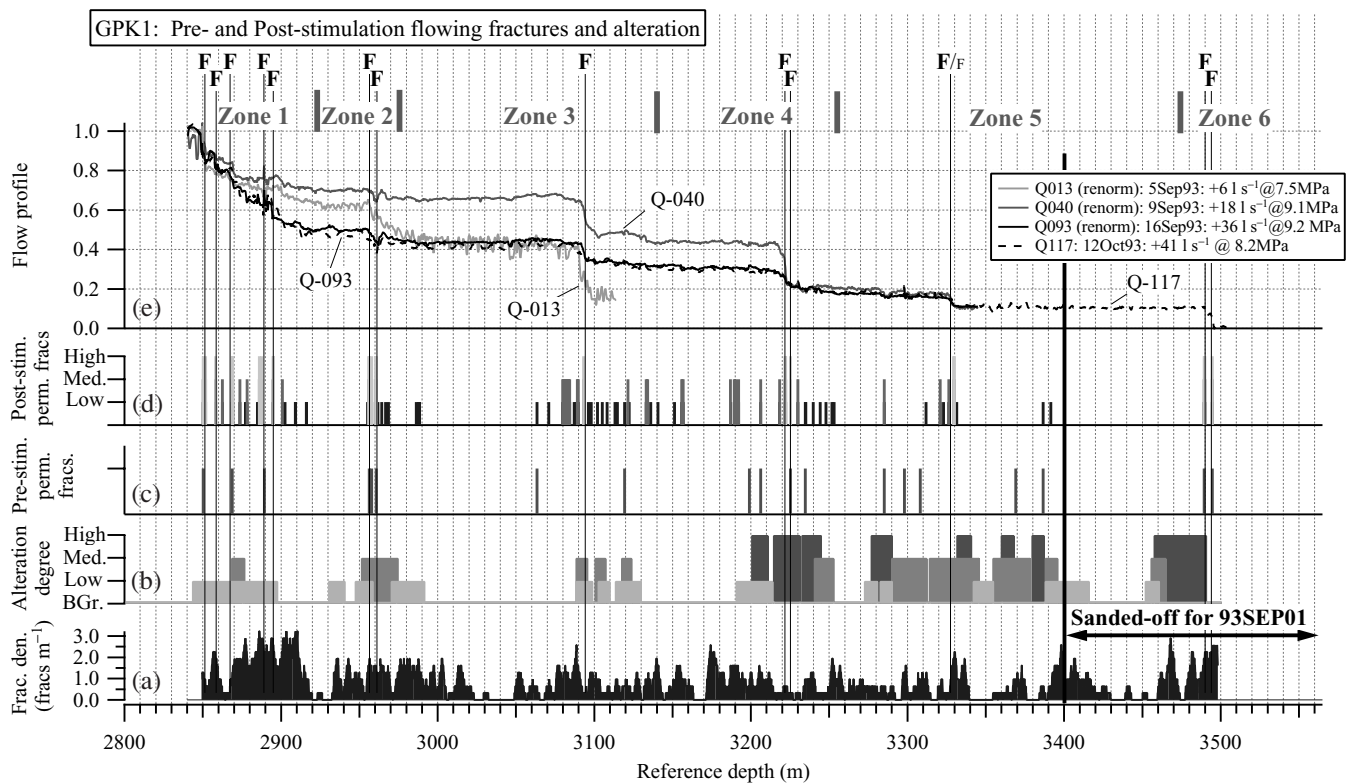
Figure 3. Summary of geological and hydraulic information for GPK1. (a) UBI-imaged natural fracture density; (b) hydrothermal alteration determined largely from cuttings; (c) location of naturally permeable fractures; (d) location and ranking of fractures that supported flow following the two stimulation injections; (e) selection of flow profiles from spinner logs run during the stimulations and post-stimulation characterization tests. The well was filled with sand to 3400 m for the 93SEP01 injection. Thus, to permit comparison of the flow profiles from this injection with later tests on the entire open hole, the 93SEP01 profiles have been normalized so as to give the same flow fraction below 3350 m as seen in the later tests. Major flowing fractures are denoted by F and their corresponding six flow zones are as indicated.

they are likely to be the more hydraulically significant. The orientation distribution of the UBI-imaged fractures is shown in Fig. 4(a). The vast majority are high angle and strike within $\pm 45°$ of N–S.

Petrological studies of core from well EPS1 suggest that the fractures can be grouped into two classes that have a different history and characteristics, and that are distinguishable by the presence or absence of hydrothermal alteration. Three alteration events are recognized as having affected the granite. The first is an early, pervasive alteration that slightly affected the entire granite and is possibly related to the cooling of the pluton. The event is associated with the development of mode 1 tension fractures that tend to be relatively narrow and filled with chlorite and calcite. The second is a later event, which produced localized hydrothermal alteration of fractures whose nature and clustered organization suggests they are the internal expression of fracturing within extensive shear structures through which much fluid flowed (Genter & Traineau 1996). The third alteration event involved haematite deposition in fractures near the top of the granite and is unimportant to this paper (Genter 1989; Sausse 2000). A typical cross-section through the hydrothermally altered shear structures is illustrated in Fig. 5 (Genter *et al.* 2000). The density of fractures within the structure is greatest at the core where fillings of illite and quartz, occasionally geodic, are prevalent. In contrast, the porosity is greatest near the peripheral contact with the protolith, reflecting leaching of plagioclase feldspars (Genter *et al.* 1998). Alteration zone widths, which are a measure of the local width of the structures, of centimetres to tens of metres are

seen in the EPS1 core (Genter & Traineau 1996). It is likely that most if not all major structures within the rock mass are of this type. The structures represent an old structural trend that was reactivated during the Tertiary (Eocene compression, Oligocene extension) and in the present-day stress field (Larroque & Laurent 1988; Dezayes *et al.* 1995; Genter *et al.* 1995). Importantly, they are high-angle and trend mostly towards $20°$NW $\pm 10°$, as shown in Fig. 4(c). These orientation estimates are derived from the EPS1 core and fracture imaging logs in wells GPK1 and GPK2, and mostly represent either the orientation of the clearest fracture visible in the alteration halo, or a statistical average of the orientations of the individual fractures in the alteration cluster, depending upon which was considered most appropriate. We assume that the averaging process is unaffected by bias and that the tendency for these structures to strike towards the NNW is real. A similar bias to NNW seen in the distribution of strikes of fractures that have large apertures on the azimuthal resistivity imager (ARI) electric log (Sausse, unpublished data). The trend to the NNW is significantly different to the strikes of the unwinnowed fracture population, which tend to be more broadly and symmetrically distributed about $10°$NW (Fig. 4a).

The profile of second-event hydrothermal alteration along the GPK1 open-hole section is shown in Fig. 3. The data are derived from analysis of cuttings augmented by limited core and thus are subject to sampling and depth errors as a result of mixing. Three levels of alteration are distinguished based essentially on the degree of development of clay minerals, notably illite, and the removal of primary minerals such as biotite and plagioclase. For the low
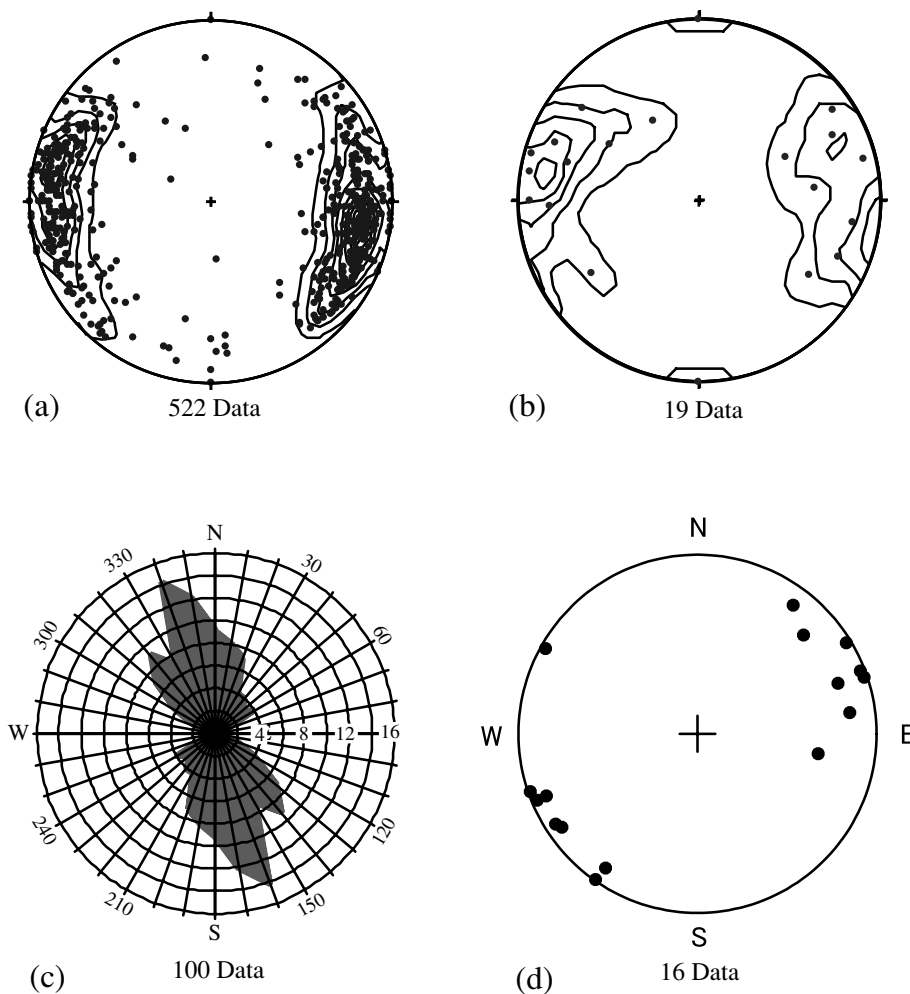
Figure 4. (a) Stereoplot showing the orientation distribution of poles to natural fractures identified on the UBI log run in the open-hole section of GPK1. (b) Poles to the subset of fractures that are permeable prior to stimulation. (c) Rose diagram showing the distribution of strikes of hydrothermally altered shear structures in the granite (see Genter & Traineau 1996, for corresponding plot of poles). (d) Stereoplot showing poles to multiplet planes of multiplet cluster E (MC-E) derived from principal component analysis. The mean/standard deviation of the dip and dip direction are $87° \pm 10°$ and $25°NW \pm 22°$, respectively. All stereoplots are lower-hemisphere, equal-area projections.
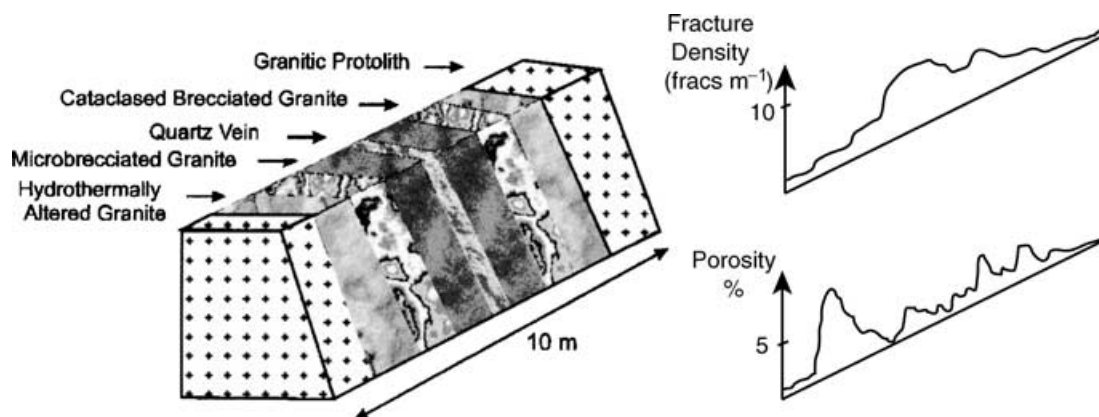

Figure 5. Cross-section through an ordered structure, which shows hydrothermal (second-event) alteration. The fracture density is a maximum at the centre, whereas the porosity is greatest at the margins where extensive leaching has taken place. The internal structure and type of alteration indicate it is a cataclastic shear zone through which significant quantities of fluid have passed. After Genter *et al.* (2000).

alteration grade, biotite is mainly altered and transformed into illite; for the moderate alteration grade, biotite and plagioclase are in the process of illite transformation; and for the high alteration grade, the biotite and plagioclase are removed and in places geodic secondary quartz deposited. Moderate and strongly altered rock is particularly prevalent in the hole section below 3200 m whereas above this depth the alteration zones are more isolated. All these zones most likely reflect intersecting shear-zone structures.

3.2 Pre-stimulation rock mass permeability

A series of low-pressure hydraulic tests were conducted to characterize the natural permeability of the granite. These indicated an open-hole transmissivity of $0.7 \, l \, s^{-1} \, MPa^{-1}$, implying an equivalent porous medium (EPM) permeability of the rock mass of $3 \times 10^{-16} \, m^2$. Spinner logs indicated that almost all flow in/out of the rock mass occurred at a prominent fault at 3490 m, which was the dominant permeable and geological structure in the open-hole section (Jung *et al.* 1995). This is emphasized by tests conducted without the fault, which indicated an EPM permeability of $2 \times 10^{-17} \, m^2$ (Jung *et al.* 1995), a value close to the mean permeability measured on intact core samples of $1 \times 10^{-16} - 1 \times 10^{-18} \, m^2$ (Rummel 1991). Estimates of average permeability derived from analysis of the growth of the microseismic cloud also suggest values in the range $-5 \times 10^{-17} \, m^2$ (Shapiro *et al.* 1999; Audigane *et al.* 2002). Despite such low transmissivity, analysis of vertical seismic profile (VSP) surveys, tube waves and a thermal log run after a low-pressure injection indicated a further 17 fractures above the fault that were also permeable (Evans 2001a). Their locations and orientation distribution are shown in Figs 3 and 4(b), respectively. Most show evidence of medium or high hydrothermal alteration, indicating they are elements of the large-scale shear structures and suggesting that natural flow through the rock mass occurs within a connected network formed from such structures (Evans *et al.* 2004).

3.3 State of stress

The stress data indicate the stress regime in the granite penetrated by GPK1 is consistent with the graben setting, but do not define whether strike-slip or normal faulting predominates. The orientation of the maximum principal horizontal stress, S_{Hmax}, obtained from thermally induced tension fractures is relatively well determined as $170°NE \pm 15°$ (Cornet & Jones 1994; Brudy & Zoback 1999; Bérard & Cornet 2003). This differs significantly from the regional trend obtained from inversion of focal mechanisms, which suggests a more NW–SE orientation (Plenefisch & Bonjer 1997). The magnitude of S_{Hmax} is taken as being equal to the vertical stress (given by the integrated overburden) because focal mechanism solutions of induced microseismic events tend to show both normal and strike-slip components (Helm 1996; Gaucher 1998; Darnet 2000). This differs slightly from the S_{Hmax} profile proposed by (Rummel & Klee 1995), which was based on hydrofracture estimates derived from the controversial re-opening method (Ito *et al.* 1999; Rutqvist *et al.* 2000) and which predicts tension fractures in the lower section of the hole that are not observed (Bérard & Cornet 2003). Two profiles of minimum principal horizontal stress, S_{hmin}, obtained from best-fitting linear trends to the results of hydraulic testing of pre-existing fractures (HTPF) tests above 2000 m (Baumgärtner & Rummel 1989) and several deeper hydrofracture tests (Klee & Rummel 1993) are shown in Fig. 6. The dotted trend is the preferred profile because it excludes the 3506-m data
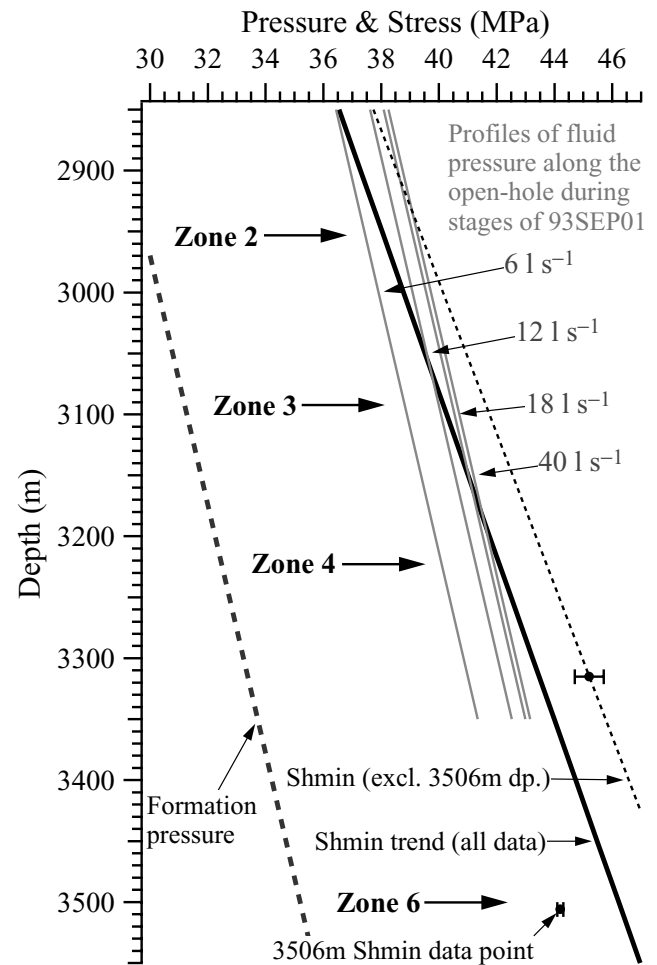
Figure 6. Profiles of minimum principal horizontal stress, S_{hmin}, derived from least-squares fits to the available data points. The solid line (Rummel & Klee 1995) uses all data points in the fitting, whereas the dotted profile excludes the data point at 3506 m where the stress state is locally perturbed. The grey lines denote the profiles of maximum pressure along the well bore during several stages of the 93SEP01 injection.

point, which probably measures a locally perturbed stress state (the test induced an E–W fracture; Klee, 2004, unpublished data). This profile is also preferred because it is consistent with the presence of drilling-induced tension fractures between 2950 and 3300 m, which did not propagate during the injections (Evans 2004), and also with hydrojacking occurring above 2950 m (Cornet & Jones 1994).

4 STIMULATION INJECTION TESTS

The first of two major stimulation injections of GPK1 was conducted in September 1993. This is denoted as 93SEP01, and was conducted with the borehole below 3400 m filled with sand leaving 550 m of open hole. The records of flow rate, wellhead and differential pressure are shown in Fig. 7. Differential pressure, ΔP, is the downhole pressure excess above ambient formation pressure and does not vary significantly along the open-hole section (Evans *et al.* 1996). The injection rate was raised in a stepwise manner from 0.15 to $36 \, l \, s^{-1}$ over a period of 16 day. Well injectivity increased rapidly from the initial value of $0.04 \, l \, s^{-1} \, MPa^{-1}$ at the end of the $0.15 \, l \, s^{-1}$ stage (ΔP of 3.9 MPa) to $0.8 \, l \, s^{-1} \, MPa^{-1}$ by the $6 \, l \, s^{-1}$ stage (ΔP of 7.6 MPa) reflecting stimulation of the rock mass. This is shown by the
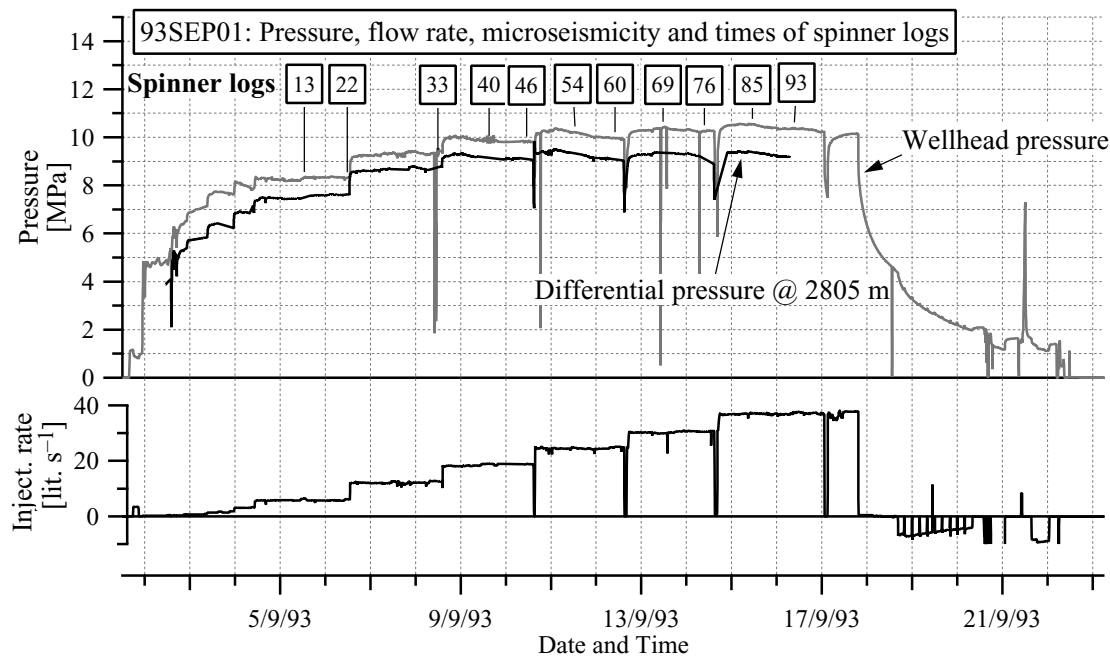
Figure 7. Pressure and flow rate records from the first stimulation injection of GPK1 when the hole was filled with sand up to 3400 m. The times of spinner logs are indicated above. Differential pressure, which is the downhole pressure excess over the ambient formation pressure (28.4 MPa at 2805 m), appears to be limited to 9.0 MPa except for small transient increases following the flow-rate increases.
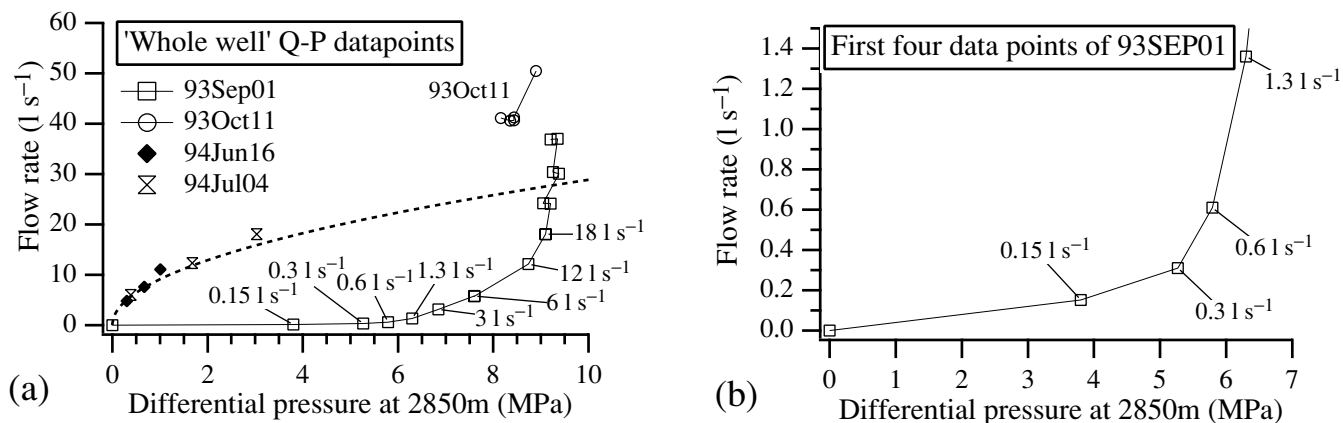

Figure 8. (a) Cross-plot of well head flow versus differential pressure prevailing at the end of each of the stages of the two major stimulation injections of 1993 and the two relatively low-pressure production (94Jun16) and injection (94Jul04) tests conducted in 1994. The pressure-limiting behaviour at 9.0 MPa is evident. The 1994 test data points define a parabola, indicating that the impedance governing fluid exchange between the well and the far field is governed by turbulent-like losses (Evans *et al.* 1996; Kohl *et al.* 1997). (b) Expanded view of the first stages of 93SEP01 showing that transmissivity increases early in the injection and accelerates when differential pressure exceeds 5 MPa.

change in slope of the flow-ΔP cross-plot in Fig. 8. Subsequently, the flow rate was increased in $6\,\mathrm{l\,s^{-1}}$ steps every 2 day. However, the resulting increases in pressure became progressively smaller, indicating pressure limiting behaviour at approximately 9.0 MPa above ambient (Fig. 8). At the end of the test, the well was shut-in for 12 hr before being vented. In all, 25 000 m^3 of fresh water had been injected and the transmissivity at 1 MPa injection pressure had increased 200-fold (Evans *et al.* 2004).

A selection of flow profiles from spinner logs run during the injections are shown in Fig. 3. Steps in the profile indicate points where significant flow enters the rock mass. The uppermost 50 m of the open-hole section includes five discrete flow points, whereas the underlying 800 m contains only a further five, which are localized

and isolated at 100–150 m intervals. Based on this distribution, the hole was divided into six sections denoted zones 1–6 whose boundaries are indicated. With the exception of zone 1, each zone contains an isolated flow point near its centre, usually composed of one or two neighbouring, occasionally complex fractures (Evans 2000). Evidently, all major flow points occur within hydrothermally altered zones (Fig. 3), suggesting that the flow penetrated the rock mass along the major shear structures.

The flow profile evolved during the injection, reflecting changes in the location of stimulation (Fabriol *et al.* 1994). The first spinner log was run during the $6\,\mathrm{l\,s^{-1}}$ stage and indicated that the majority of flow entered the rock mass in the upper half of the open-hole section (Fig. 3). However, transmissivity at that time was increasing faster

at the deeper levels so that by the $18 \, \mathrm{l \, s^{-1}}$ stage the majority of flow entered below 2950 m. Thereafter, this trend reversed so that by the end of the injection, some 60 per cent of the injected fluid entered the rock mass through the zone 1 fractures (Jones *et al.* 1995). Thus, early-time stimulation was most effective below zone 2. An important observation is that the flow profile prevailing at the end of injection was largely preserved during subsequent high- and low-pressure injections. This indicates that the fracture aperture changes underlying the transmissivity increases were permanent and hence that the fractures were propped open through some mechanism or other.

After the sand was cleaned out and an injection performed on the fault at 3490 m (93OCT01), the second major injection was conducted (93OCT11), this time on the entire hole. Flow rate was kept constant at $40 \, \mathrm{l \, s^{-1}}$ for 4 day before being increased to $50 \, \mathrm{l \, s^{-1}}$ for the final day. At the end of the 40 and $50 \, \mathrm{l \, s^{-1}}$ stages, the downhole pressures exceeded ambient by 8.4 and 8.9 MPa respectively, somewhat less than the 9.1 MPa prevailing at the end of the $36 \, \mathrm{l \, s^{-1}}$ stage of 93SEP01 (Fig. 8). Thus, some changes had taken place within the rock mass during the shut-in period, which served to increase transmissivity. Because microseismic activity was low during this period, the underlying processes were aseismic (Evans 1998). Nevertheless, the flow profile remained largely the same as prevailed at the end of the 93SEP01 injection (Fig. 3).

In the following year, a low-pressure production and injection test were carried out to evaluate the efficacy of the stimulation injections. These are described below in some detail because they have bearing on the interpretation of the microseismicity induced during 93SEP01.

5 POST-STIMULATION CHARACTERIZATION TESTS: EVIDENCE FOR LINKAGE BETWEEN MAJOR FLOW PATHS

Evidence that the flowing fractures in zones 2 and 4, some 250 m apart, were linked within the formation by a low-impedance flow path was obtained from flow logs run during the two 1994 stimulation-characterization tests. The first was a step-pressure production test (94JUN16) and the second a step-rate injection test (94JUL01; Fig. 9a). Pressures in both tests remained relatively low. Spinner logs were run at two different flow rates in each test to determine the flow profiles shown in Fig. 9(b). A systematic difference in the flow profile is evident between injection and production conditions, with proportionally more of the fluid entering the rock mass at zone 2 during injection than was produced during production and the converse for zone 4. The same asymmetry was also seen in later tests (Evans *et al.* 1996). Importantly, the change in flow distribution did not affect the hydraulic impedance of the borehole: that is, the flow into the rock mass for a given positive differential pressure was the same as produced from the hole for the same drawdown. This is evident in Fig. 10(a) where the flow component entering/leaving the rock mass over each of the six zones at the time of the logs is plotted against the prevailing differential pressures. Steady-state conditions are approached at the times of the logs. Thus, the six cross-plots describe the pressure-dependent impedance characteristics of each of the zones. Both production and injection data are plotted in the same quadrant, which is sensible provided the impedance is symmetrical. The cross-plot for the entire well in Fig. 8 confirms this symmetry and shows that differential pressure varies as the square of flow rate, thereby implying that the net impedance governing flow

is dominated by turbulent-like losses (Jung *et al.* 1995; Kohl *et al.* 1997). The data for zones 1 and 6 in Fig. 10(a) also define parabolas consistent with a turbulent-like impedance that is symmetrical for production and injection. In contrast, the data points for zones 2 to 5 are disjointed and highly asymmetric. However, when these zones are treated as one by summing their flow contributions, the data points for both production and injection fall on a single parabola (Fig. 10b). This demonstrates that, although positive and negative differential pressures of the same magnitude generate the same net throughput of fluid through the paths that exit at the flowing fractures of the well, the flow is distributed between them differently. Such behaviour indicates that flow points are hydraulically connected by relatively conductive flow paths whose flow fractions are not stable. Moreover, it indicates that the source of the impedance that controls fluid exchange between the borehole and the far field lies outside this connected network, because otherwise an impedance change would accompany the flow redistribution. The hydraulic conceptual model suggested by these results is shown in Fig. 11. The primary redistribution occurs between the flow points of zones 2 and 4, which, it will be seen, lie near the top and bottom of a major microseismic structure.

Further evidence that supports the conceptual model comes from temperature logs run after the 93SEP01 stimulation, which suggests that the flow path connecting to the hole through the zone 2 flowing fractures extends downwards (Fig. 12). During the injection, the well bore had been cooled by the injected fluid to a relatively uniform temperature of 30–40 °C. Log T097 was run 1 day into the shut-in period at the end of injection. A sharp, warm peak of some 5 °C can be seen superimposed on larger-scale trends at the depth of the zone 2 flowing fractures. This reflects the ambient flow of relatively hot fluid within the fractures either across the borehole, or into the borehole itself. The fact that the fluid is hot suggests it is flowing upwards from below. Similarly, temperature logs run during the venting that followed shut-in showed that the zone 2 fractures produced fluid that was hotter than the borehole fluid, whereas most other fractures produced relatively cold fluid (Fig. 12). The latter is more expected because the fluid in the borehole was moving upwards from depth and thus tends to be relatively hotter than the borehole wall, which is still cooled (Evans *et al.* 2004).

In summary, the temperature log evidence suggest that zone 2 fractures connect to a permeable structure that leads downwards, and the flow-diversion behaviour indicates that zone 2 and zone 4 fractures are connected by a low-impedance flow path.

6 MICROSEISMIC OBSERVATIONS

The microseismicity induced during the 1993 test series was recorded on a downhole network consisting of a single, four-component accelerometer sonde placed at the bottom of each of the three seismic observations wells and a hydrophone in well EPS1 (Fig. 2). The seismic network lies directly above the induced microseismicity and has an aperture of only 2 km. Thus, the location error ellipsoid is approximately oblate, with vertical and horizontal standard errors of 20 and 50 m, respectively. Sampling of the focal sphere is too poor to constrain focal mechanism solutions from downhole first-motion data alone. The data acquisition system was triggered and waveforms digitized at 5 kHz. The total bandwidth of the data is 10–2500 Hz. However, the vast majority of signals had little energy above 800 Hz. The downhole network was active more or less continuously from 1993 August to 1994 February.
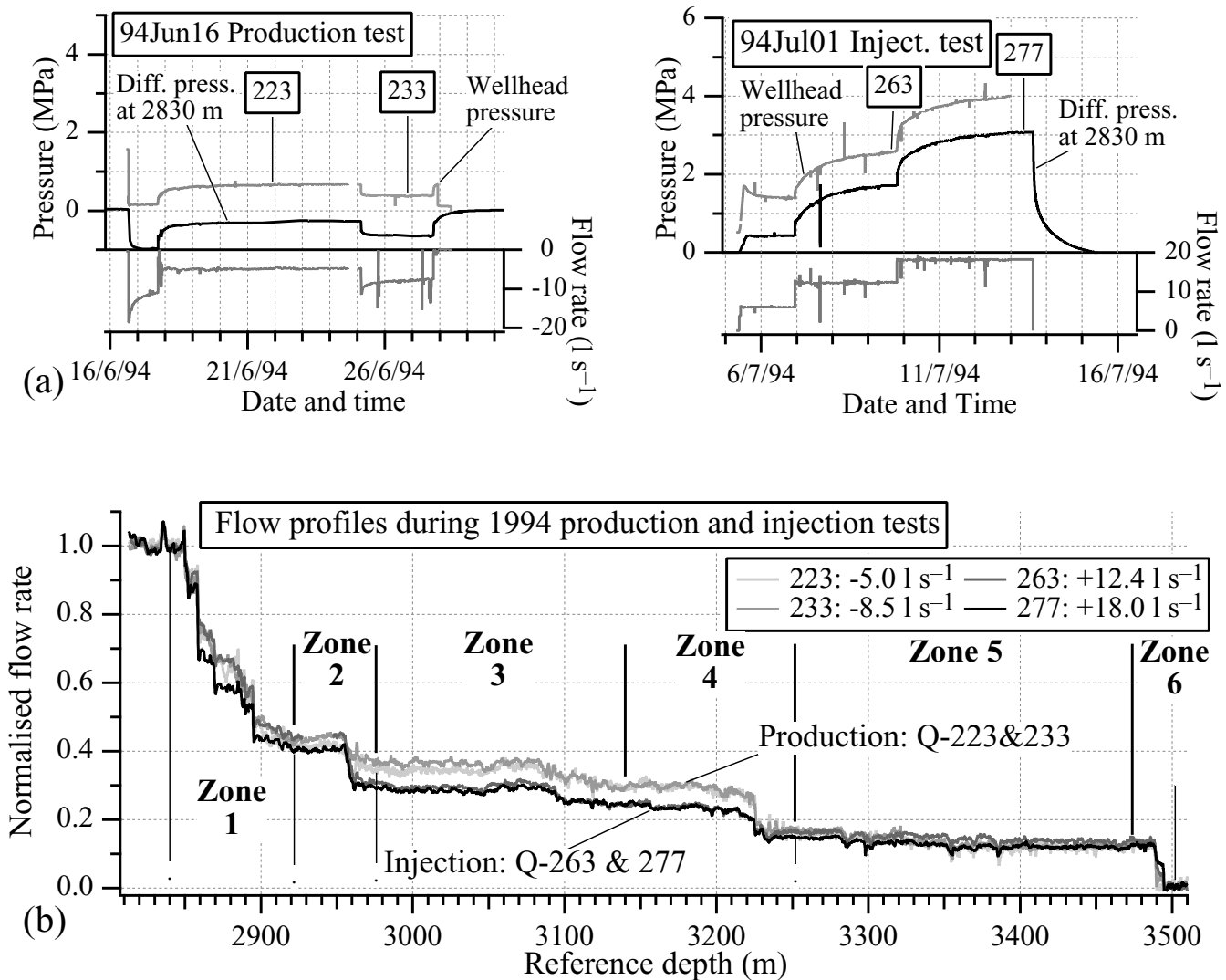
Figure 9. (a) Test records of the 1994 production and injection tests. The numbers denote the times at which the spinner logs in (b) were run. (b) Flow profiles derived from the spinner logs which were all run under approximately steady-state conditions. The zones into which the well is divided in most cases contain a single dominant flowing fracture indicated by a step. The profiles from the production test (shown in lighter greys) differ systematically from those from the injection test primarily between the flowing fractures in zones 2 and 4.

The first test that produced detected seismicity (designated as 93AUG19) was a small volume injection performed through a packer at 3560 m on the lowermost 40-m open-hole section below the fault at 3495 m. The small interval makes this test ideal to test location accuracy. The first events were observed at differential pressures in the range 4.0–7.5 MPa. The JHD locations of these events obtained using the model described in the next paragraph lay within 50 m of the injection interval, consistent with the error estimates.

Some 12 000 events were recorded during the 93SEP01 injection with moment magnitudes ranging between −2 and 1 (Jones & Evans 2001). The first occurred some 17 hr after the start of injection near the zone 2 flowing fractures when the differential pressure increased above 5 MPa. Some data loss occurred during the 12 and 24 l s^{-1} injection stages as a result of tape damage. Source parameter estimates indicate the largest event had to a moment of at least 4×10^{10} N m (Jones & Evans 2001). The JHD locations of the events obtained from the four *P*- and three *S*-wave arrival times are shown in Fig. 13(a). The inversion assumed straight ray paths with *P* and

S velocities and station corrections obtained from a calibration shot conducted in GPK1 at 2945 m measured depth. The standard error in picking arrival times is estimated as 2–3 ms. The systematic error in location as a result of the neglect of velocity variations is negligible near the shot point but increases with distance. Studies using models that employ velocities consistent with sonic logs suggest the systematic component of the error is likely to be less than ±30 m for events at the periphery of the cloud (Dyer *et al.* 2001). The JHD locations in Fig. 13(a) define a diffuse, subvertical cloud of approximate dimensions 0.5 km wide, 1.2 km long and 1.5 km high and oriented 25°NW, with little evidence of internal structure.

6.1 Collapsed locations

As a first step in image processing, the collapsing algorithm of Jones & Stewart (1997) was applied to the JHD locations. Collapsing is a statistical optimization technique that attempts to reverse the effects of random errors, which cause nearby locations to spread apart. The technique is iterative: for each location in turn, the centre of
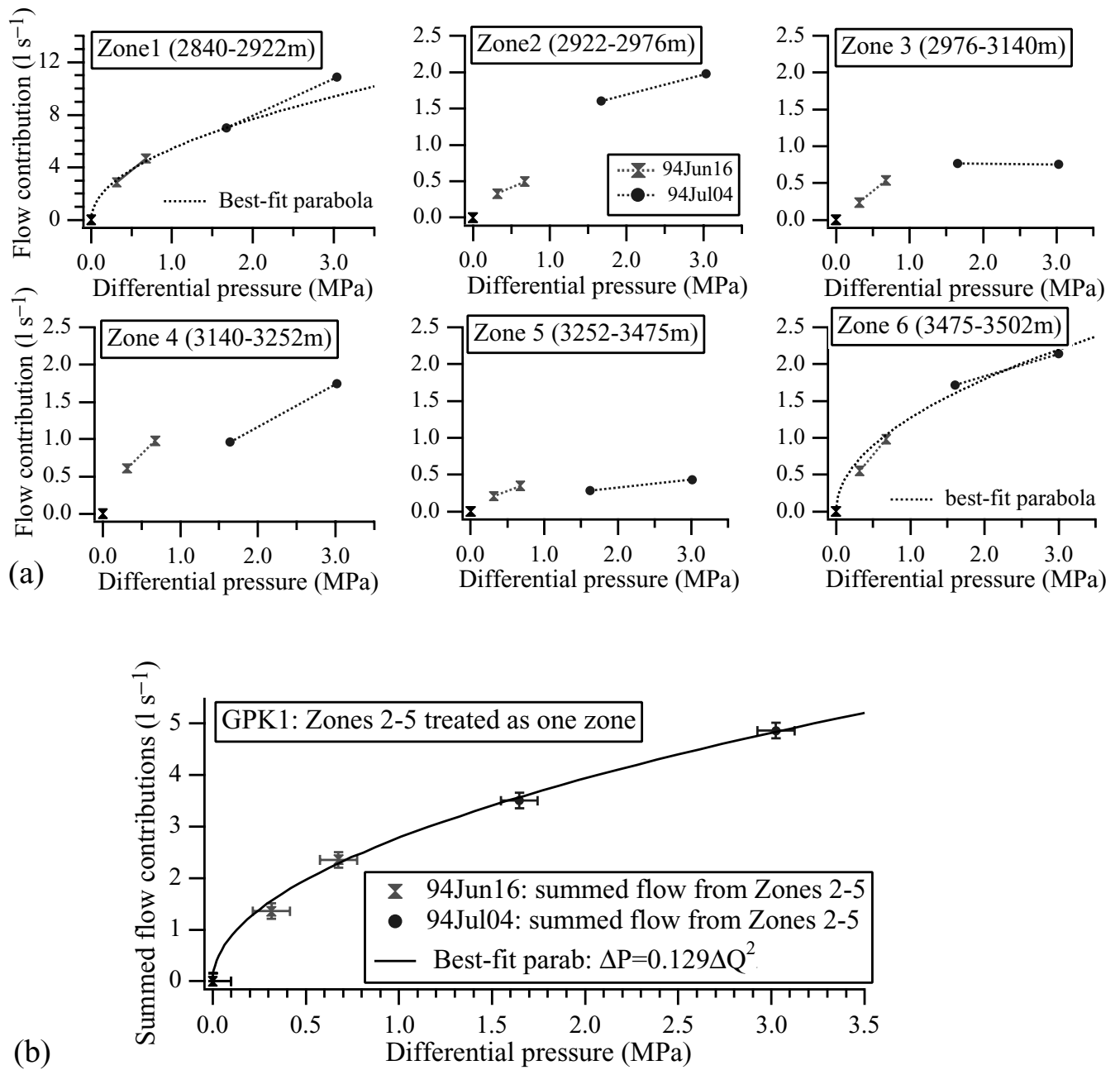
Figure 10. (a) Plots of flow entering/leaving the rock mass estimated from the profiles in Fig. 9(b) versus the differential pressure at the zone at the time of the log. Both production and injection data points are plotted in the same quadrant. The collective data from zones 1 and 6 are well-fitted by a parabola, whereas the production and injection data points for the other zones are disjointed. However, when these are treated as a single zone by summing their flow contributions, the data define a parabola as shown in (b). Thus, although the distribution of flow between zones 2–5 is different for injection and production, the net impedance is the same.

gravity of all the locations that lie within its uncertainty ellipsoid is found and the location is moved a fraction towards this point. In this way, a new generation of events is formed. The frequency distribution for movements is computed. This process is then repeated until the frequency distribution most closely matches a chi-squared distribution with 3 degrees of freedom, which is the expected uncertainty distribution in three dimensions for uncertainties obeying normal statistics (Jones & Stewart 1997). In essence, the process assumes that two events whose error ellipses overlap are more likely to be nearer together than farther apart. The method is well suited to removing the blur that tends to obscure the structures within the cloud, but is unlikely to resolve structures smaller than the error ellipsoid. The results of applying collapsing to the JHD locations are shown in Fig. 13(b). The cloud is now seen to be composed of distinct structures, most of them linear but some planar. The source animation for Fig. 13(b) showing the evolution of the cloud in 10 hr time steps is provided as supplementary material to this paper (file Soultz_93SEP01_Coll_FullCloud.rm). From this video it can be seen that the structures extend in a coherent manner. One of the largest structures is a 300-m-long tube that extends down from the vicinity of the zone 2 flowing fractures to the depth of zone 4. Close-up JHD and collapsed images of this structure are shown in
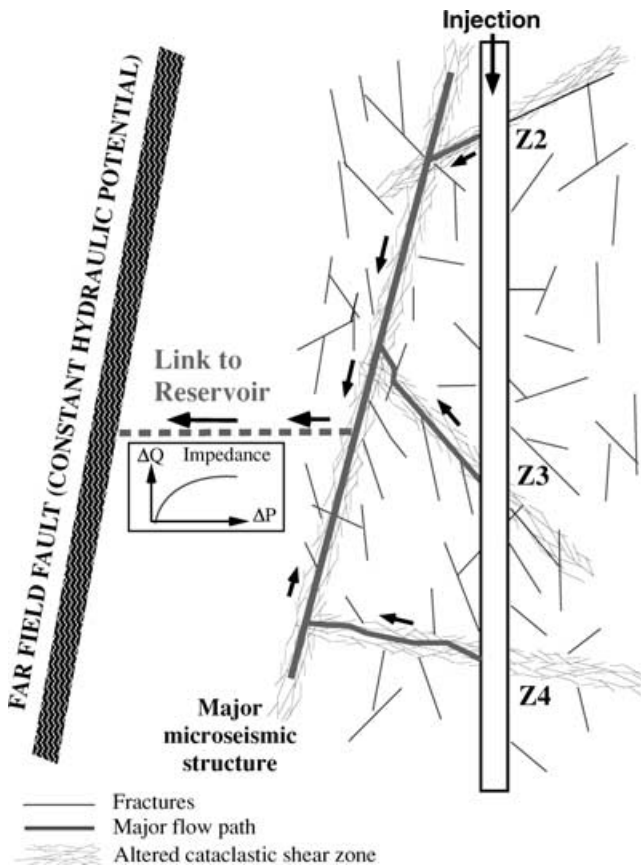
Figure 11. Conceptual model of the flow system within the rock mass in the depth range of flow zones 2–4. The flow zones at the borehole are all connected by low-impedance flow paths defined within the network of stimulated fractures of cataclastic shear zones, but the flow paths are linked to the far field through a path that has a relatively high, turbulent-like impedance. The major flow path shown between feeder paths coincides with a major microseismic structure. Modified from Evans (2000).

Figs 14(a) and (b), respectively. The structure dips at 75° to 335°NE and hereafter it will be referred to as the Evans Line (EL) structure. An animation showing the evolution of this structure in the collapsed images is also provided as supplementary material (file Soultz_93SEP01_Coll_ELstruct.rm).

7 DEVELOPMENT OF THE EL STRUCTURE

The development of the EL structure is illustrated in Figs 15 and 16. Fig. 15 shows a selection of snapshots of cumulative microseismicity viewed from the same direction as Fig. 14(b-3). The time below each frame denotes hours since the first seismic event was detected. Fig. 16 shows the time history of events within the structure as a function of depth, together with the injection pressure and flow rate records. The times of the snapshots of Fig. 15 are indicated, as are the times of temperature and flow logs, which indicate where flow was entering the rock mass. Events are considered to be part of the structure if their collapsed locations lie within 60 m of its central axis (Fig. 17a). The first events were observed after the injection rate was stepped from 0.15 to 0.3 l s^{-1} and the differential pressure increased beyond 5.0 MPa, consistent with the threshold of 4.0–7.5 MPa seen in the test 93AUG19 at the bottom of the hole. Transmissivity increases also accelerate at this pressure (Fig. 8). For convenience we take the time of the first event as zero. The early events all scatter within 50 m of the flow inlet at zone 2 (Fig. 16). After some 30 hr, the seismically active volume has spread only 100 m in all directions. A temperature log (T-001) run at this time indicates significant flow into the rock mass near the casing shoe and at the zone 2 flow point (Fig. 18). After 40 hr, the first events begin to appear along the eventual trajectory of the structure, and the rock volume between it and the borehole. Sharp changes in the gradient of the temperature log T-05 run at this time indicate that deeper flow points at zone 3 and below zone 4 had by now also become active (Fig. 18). By 60 hr, the EL structure is clearly distinguishable to 3150 m and log T-10 run just after this time indicates zone 5 at the bottom of the open hole had begun to accept flow (Fig. 18). After 70 hr, microseismic activity along the structure becomes particularly intense around 3220 m (Figs 15 and 16). These events, circled in Fig. 14(b), belong to plane 4 of the lower cluster of Phillips (2000) to be described later. By 90 hr, the outline of the EL structure had essentially reached its final form. Subsequent events largely served to increase its definition. The downward migration of microseismicactivity is also evident in the plots of cumulative seismic moment release shown in Fig. 17(b), which will be discussed later.

Examination of the migration of early microseismic events in Fig. 16 shows that they advance along the EL structure in steps that correlate with steps in flow rate but with an approximately 2 hr
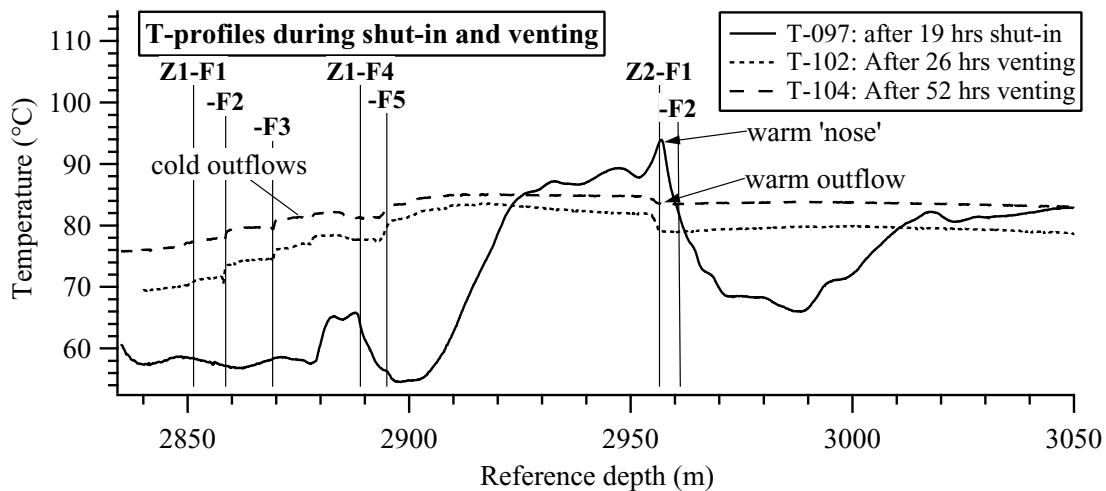

Figure 12. Temperature logs for zones 1 and 2 run during the shut-in and venting that followed the 93SEP01 injection.
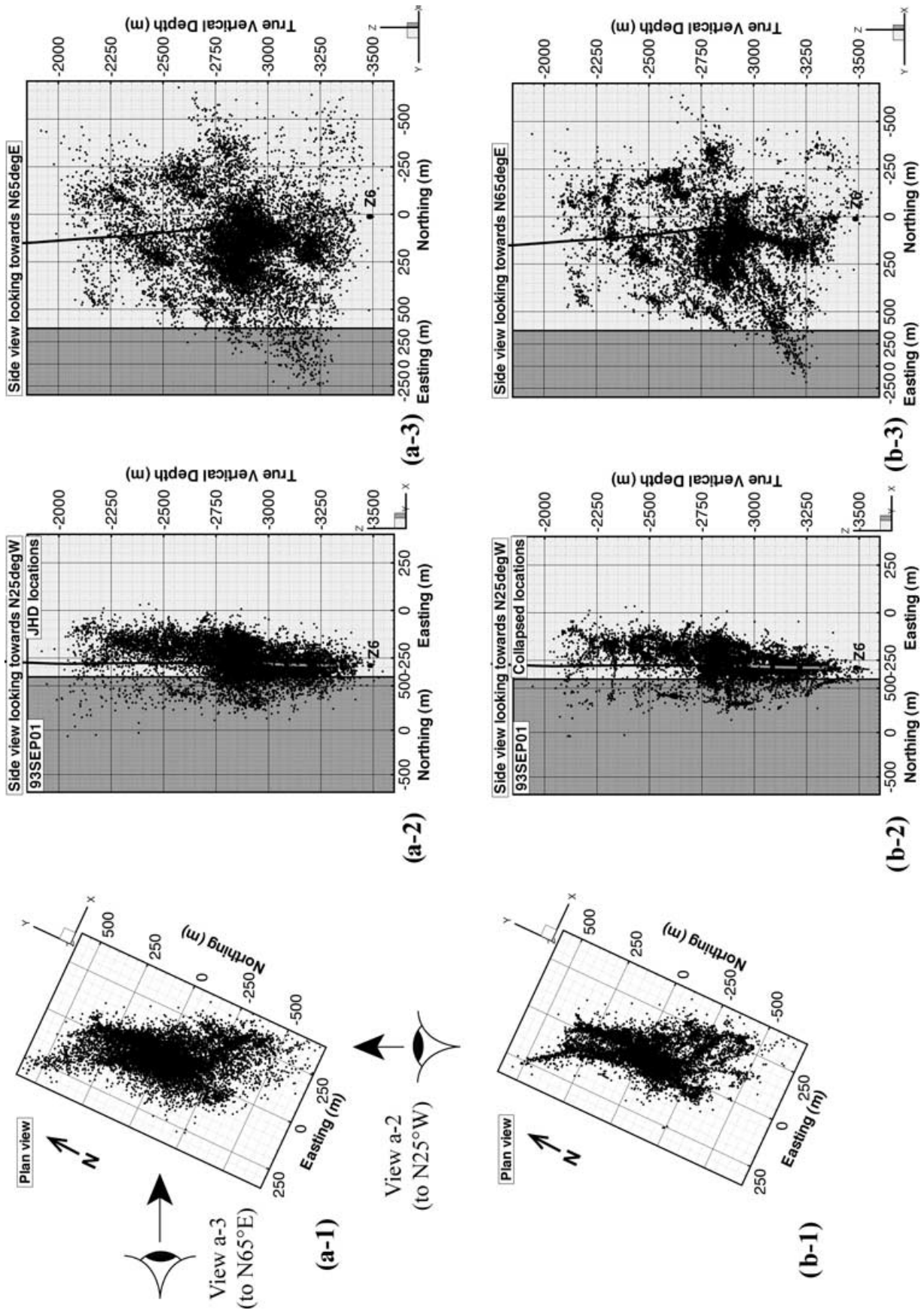
Figure 13. (a) Views of JHD locations of the full cloud. The left frame is the view from above with the well head at the coordinate origin. The centre and right frames are horizontal projections viewed from the directions shown in the left frame. (b) Locations after application of collapsing.
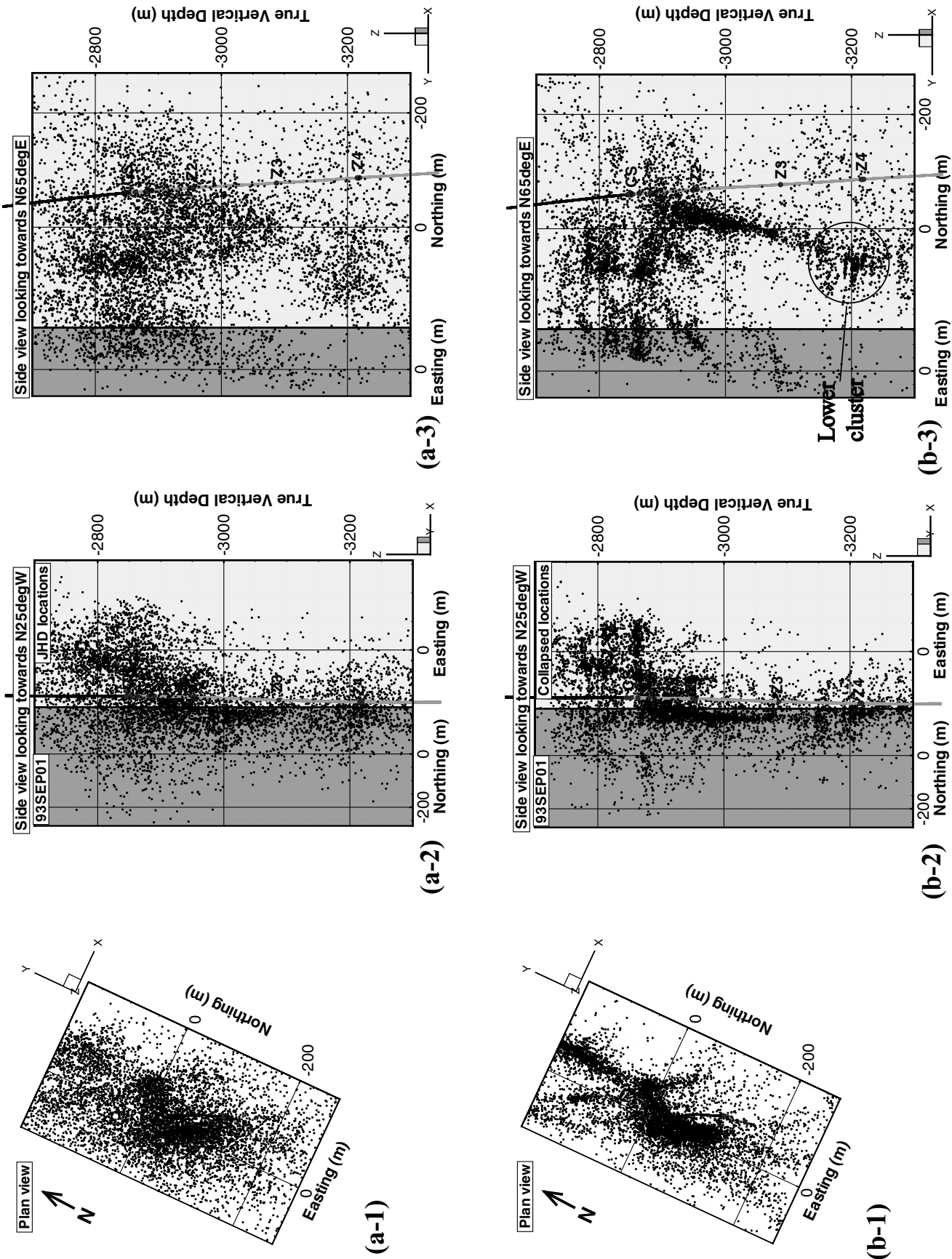
Figure 14. Geometry of the lower part of the microseismic cloud obtained by (a) JHD and (b) applying collapsing to the JHD locations. The collapsing reveals a large tubular structure beginning in the vicinity of flow zones 1/2 and extending some 300 m downwards at a dip of 75° to 335°NE to the level of flow zone 4. cs denotes the casing shoe and z2, z3, etc. denote the location of the major flowing fractures in their respective flow zones. The circle at the foot of the structure in frame b-3 denotes the lower cluster analysed by Phillips (2000).
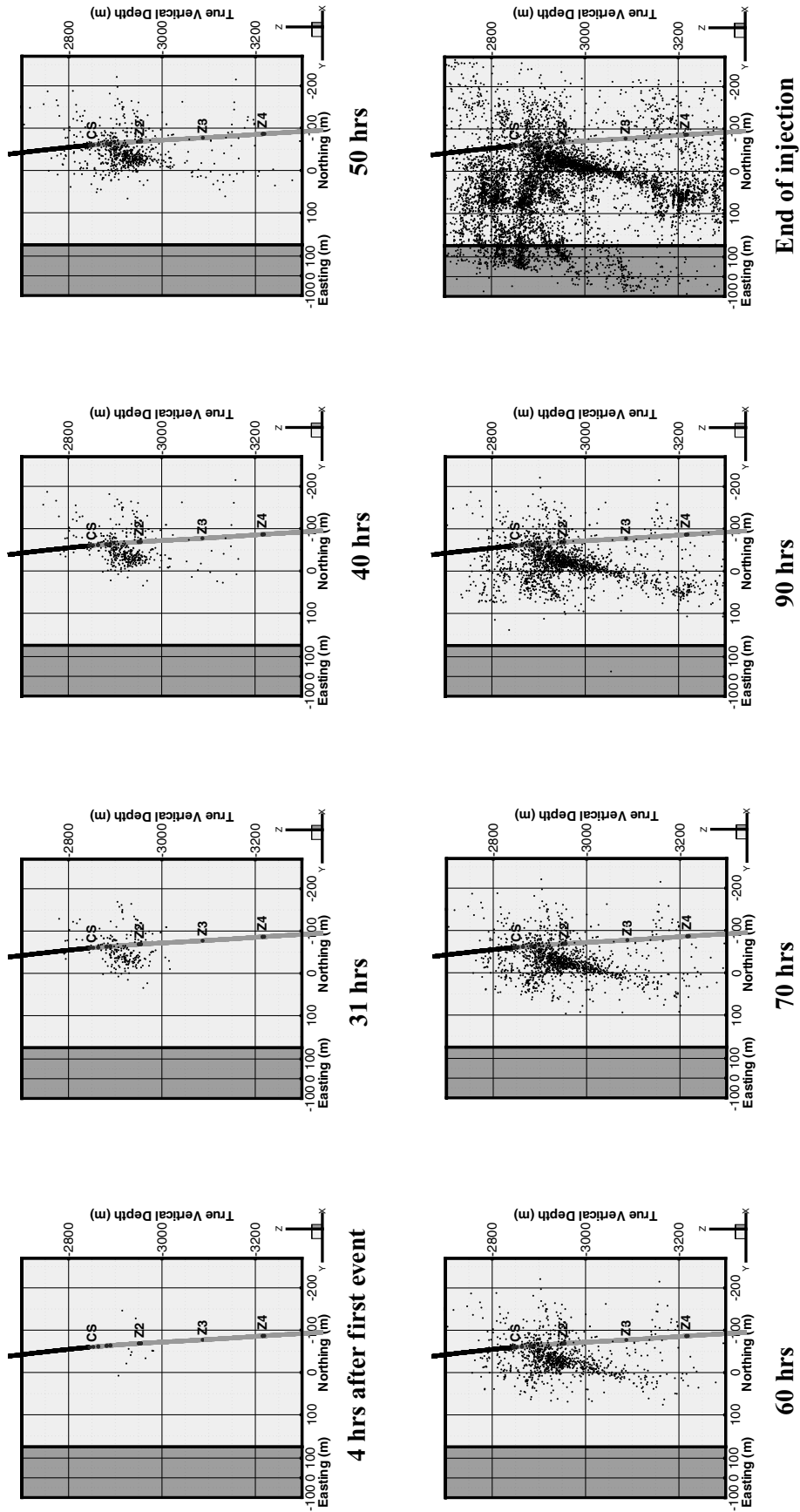
Figure 15. Frames showing the evolution of the lower part of the microseismic cloud (collapsed locations). The times of the frames represent hours after the first seismicity was detected at 16:19:11 h on 1993 September 2. The view is horizontal looking towards 65°NE.
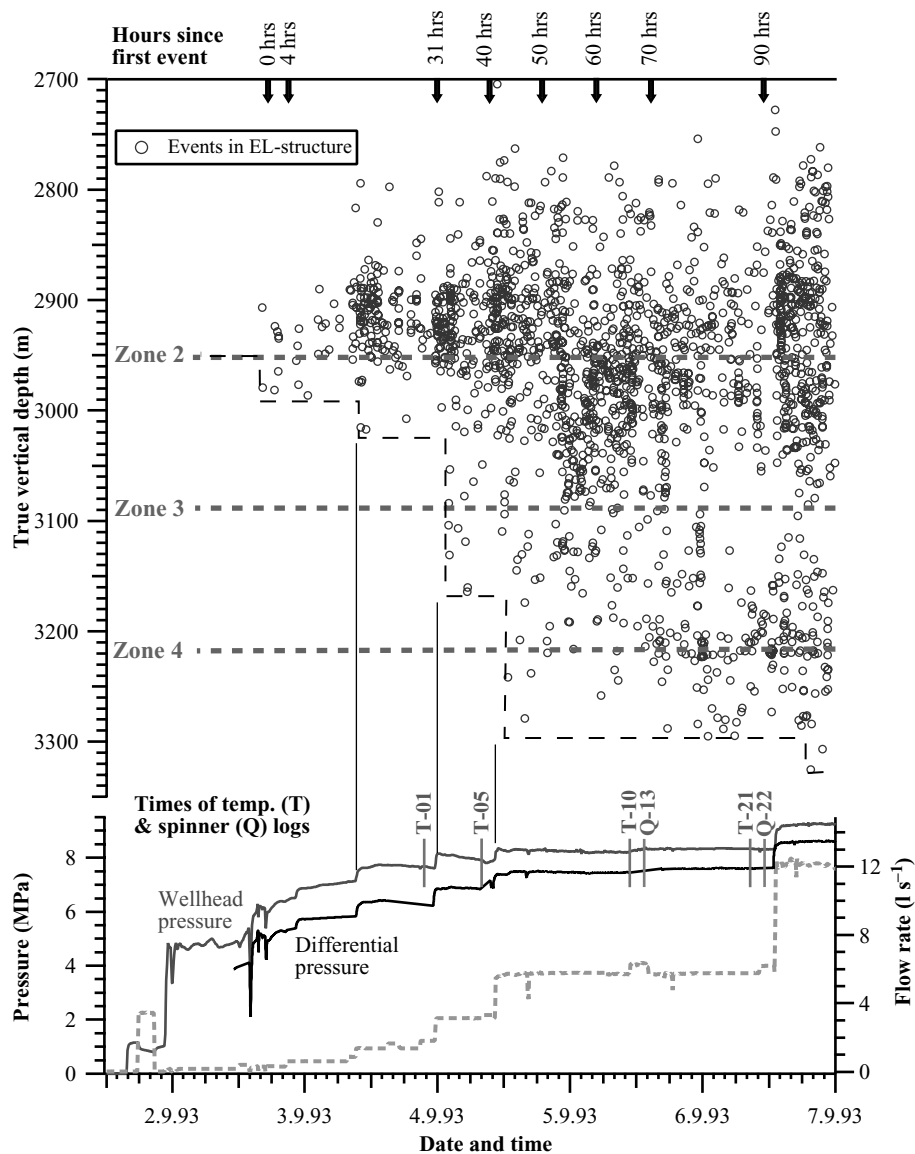
Figure 16. Advance of microseismicity along the structure in relation to the well head pressure and flow rate. The seismicity plotted is delineated in Fig. 17(a) and appears to migrate in steps that follow increases in injection rate by some 2 hr. The arrows at the top denote the time of the snapshots of the evolution of the microseismic structure shown in Fig. 15. The times of the first few temperature and flow logs are indicated on the pressure curves.

delay. Whilst the event density is too sparse to resolve details, there is little doubt that the increases in flow rate at the end of the 1.5, 3 and 6 l s^{-1} stages are all followed a few hours later by bursts of events in the region ahead of the temporarily stable microseismic front. All these steps in flow rate were accompanied by increases in downhole pressures to levels not seen previously, the peak differential pressures for the 1.5, 3.0, 6.0 and 12.0 l s^{-1} stages being 6.4, 6.9, 7.5 and 8.5 MPa, respectively (Fig. 16). These observations suggest that the bursts of seismicity are associated with the penetration of a pressure front down the structure and that the principal hydraulic connection to the borehole is at the zone 2 outlet. This was the first zone to take detectable flow, it lies at the centre of the first detected microseismic events and the hydraulic evidence indicates that the flow path it connects to leads downwards. It is also possible that the sparse seismicity seen in the rock mass between the structure and the borehole reflects flow across to the structure from the deeper flowing fractures at zones 3 and 4, which became active during the 3 l s^{-1} stage. In any case, the development of the EL structure imaged by the

collapsed locations suggests it is a continuous geological structure that presents a path for pressure to penetrate the rock mass. Given the evidence that zones 2 and 4 are connected by a low-impedance flow path within the rock mass, it is probable that the 300-m-long EL microseismic structure illuminates the primary geological structure responsible for this hydraulic connection, as illustrated in Fig. 11. In the following, we employ high-resolution microseismic imaging techniques to attempt to identify its microstructure and geological nature.

7.1 High-resolution microseismic images of microstructural elements of the structure

To resolve the nature of the microstructural features that generate the microseismicity requires a higher relocation accuracy than given by the collapsing method. Various techniques are available that differ fundamentally from collapsing in that they are deterministic rather than statistical. We have applied doublet/multiplet analysis
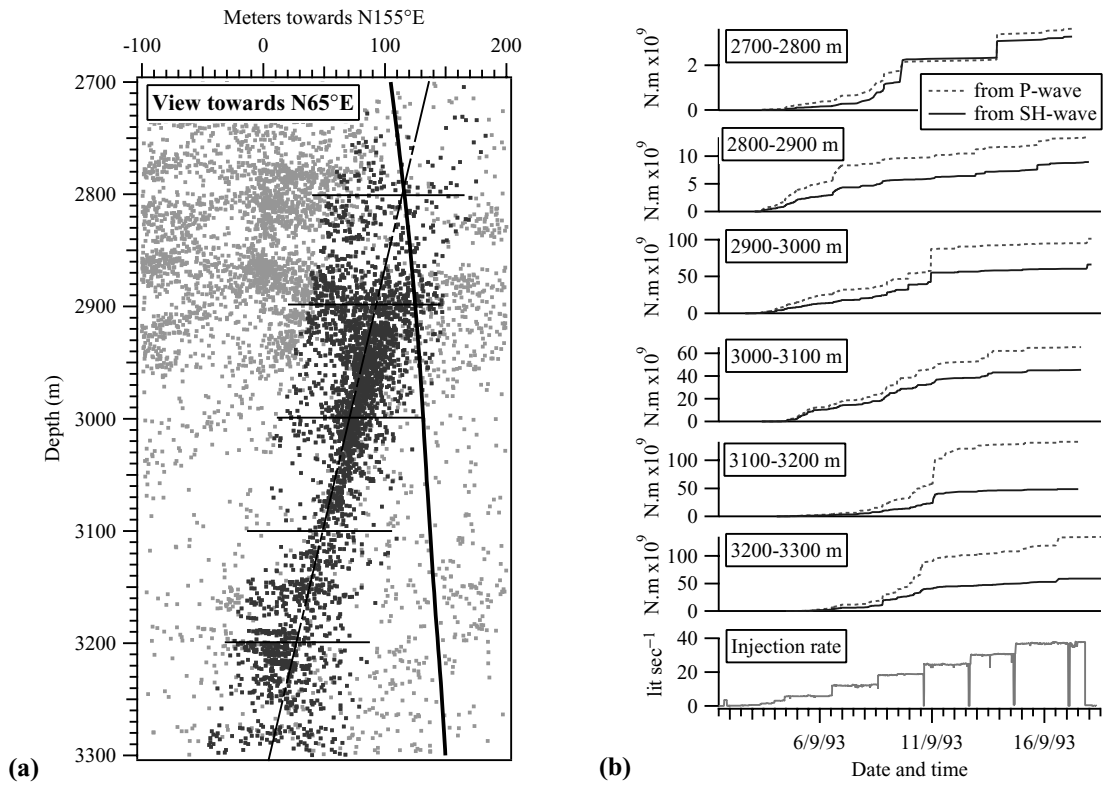
Figure 17. (a) Delineation of events in the collapsed cloud that are considered to be part of the structure. These events are shown in grey and all lie within 60 m of the axis shown. The bold line to the right is the well bore. (b) Cumulative moment release curves for 100-m sections of the structure derived from *P* (dotted) and *SH* waves. The moment estimates are lower bounds obtained by assuming a radiation geometry factor of unity. Adoption of factors averaged over the focal sphere would lead to an increase in the moment estimates by a factor of approximately 2 (Jones & Evans 2001).
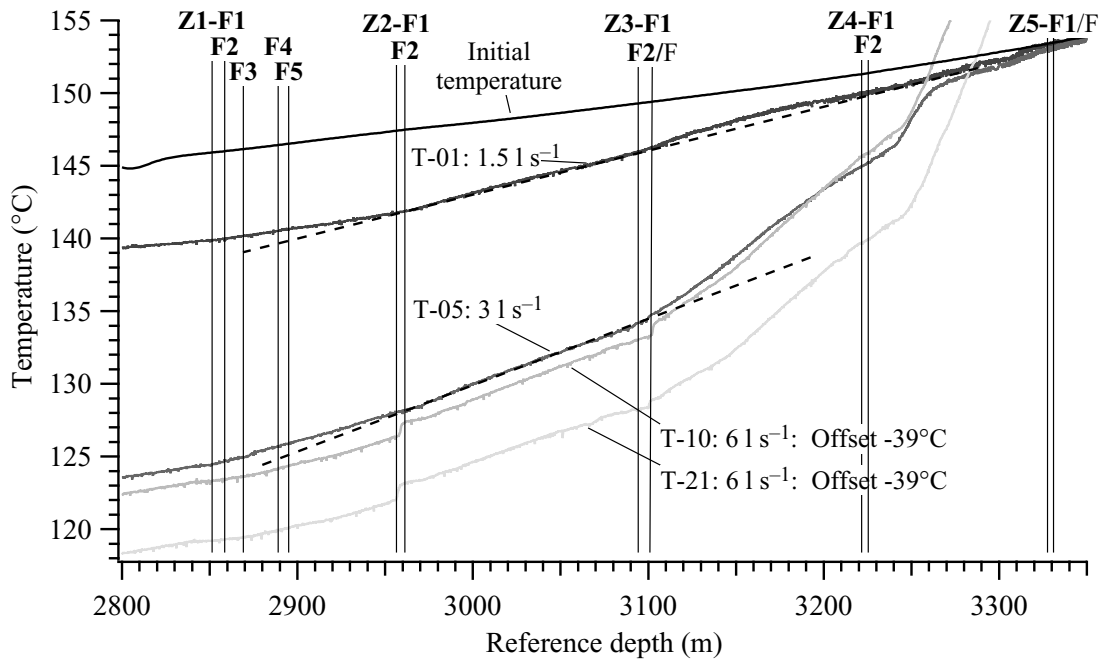

Figure 18. Temperature profiles from the first five logs run during 93SEP01. Slope changes and steps indicate points where flow enters the rock mass. The first log (T-01) was run during the $1.5\,l\,s^{-1}$ stage and shows a clear change in slope at flow zone 2 (a dashed line has been fit to the deeper section to reveal the slope change), indicating the zone was taking significant flow at this time. Subsequent T-logs indicate deeper flow zones becoming active (the two T logs run during the $6\,l\,s^{-1}$ stage have been offset by 39 °C).

(Poupinet *et al.* 1984), clustering analysis (Phillips *et al.* 1997) and multiplet-clustering analysis (Moriya *et al.* 2003). All seek to improve the relative location accuracy of events by reducing the error in the analysts' picks of the *P* and *S* onset times. This can be done for groups of events that have sufficient similarity in the waveforms such that they can be aligned and the relative onset times of the phases at each station determined with improved accuracy. The three methods we applied can be briefly summarized as follows.

(i) Multiplet analysis: in cases where the waveforms were almost identical (i.e. coherence > 0.68), cross-spectral methods of time delay estimation were used (Poupinet *et al.* 1984; Fréchet *et al.* 1989). Gaucher (1998) applied the method to the shallower part of the 93SEP01 cloud above 2900 m and identified several multiplets that defined planes that he attempted to associate with fractures at the borehole (see also Gaucher *et al.* 1998). Moriya *et al.* (2001, 2002) analysed the complete cloud of 12 000 events and found that 60 per cent belonged to some multiplet or other. Of these, 1027 events belonging to 115 multiplets which had between 5 and 29 members were relocated. The relative location error between events in a multiplet is estimated to be typically less than 1 m (rms residual error of 0.1 ms). Principal component analysis applied to the events in each multiplet showed that their locations usually defined near-planar structures with maximum dimensions of 2–12 m.

(ii) Cluster analysis: groups of events whose waveforms are not sufficiently similar to allow multiplet analysis but that have common features such as peaks that can be aligned may be suitable for cluster analysis (Phillips *et al.* 1997). Phillips (2000) applied the method to a cluster of events that lay at the bottom of the EL structure (circled in Fig. 14b). After low-pass filtering with a 50–100 Hz cut-off, three groups of similar waveforms defining clusters were found. Relative arrival times between cluster members were determined by visually aligning the common feature and yielded location errors of approximately 5 m. This structure will be discussed shortly.

(iii) Multiplet cluster analysis: this is a hybrid of multiplet and clustering analysis that allows the relative locations between multiplet groups to be improved. Although events within a multiplet have relative location accuracies of 1 m, the relative location between multiplets remains that of the error ellipsoid (up to 50 m). This can be improved if the characteristic waveforms between two multiplets have common features that allow clustering analysis to be used to locate the groups with respect to each other. Moriya *et al.* (2003) applied the method to the 115 multiplets with 5 or more members and found that most fell into 7 multiplet clusters. The location accuracy between multiplets within a cluster was estimated to be better than 5 m. However, the relative location of the clusters with respect to each other remains that of the JHD error of 50 m.

Multiplet clusters that fall in or near the upper part of EL structure are shown in Fig. 19 together with the collapsed cloud. The view is horizontal from 150°NE, the direction that minimizes the width of both the collapsed cloud and the individual multiplet structures. The latter are mostly subvertical and thus show as subvertical streaks whose colour denotes the multiplet cluster to which they belong. Recall that the relative locations of events within a multiplet are accurate to ±1 m whilst the locations between multiplets of the same colour are accurate to ±5 m (Moriya *et al.* 2003). Multiplet cluster E (MC-E) extends more than 100 m vertically down the EL structure where it is most strongly defined, from just below the zone 2 flow points to near zone 3. A detailed view of this multiplet cluster is shown in Fig. 20. The multiplet planes define a vertical structure that is 20 m wide, 75 m long and strikes 150°NE. Thus, the multiplets indicate that the EL structure is a narrow planar slab rather than the

tube suggested by the collapsed image. The orientation distribution of the multiplet planes is shown in Fig. 4(d). Most are subvertical and have strikes that range within ±25° of parallel to the main structure.

The 20 m width of the MC-E structure suggested by the plan view in Fig. 20 may in part be a result of deviations from planarity (waviness) of the geological structure that hosts the failure planes. However, the close-up of part of the multiplet cluster in Fig. 21 shows two multiplet planes that lie directly adjacent to each other but approximately 7 m apart. Thus, at this location at least, there are two, distinct, parallel, seismically active planes within the structure. The event radii in this figure are derived from the corner frequency of *SH* waves (Jones & Evans 2001) and we assume that the orientation of the slip plane of the individual events coincides with that of the multiplet plane. This is justified by the similarity of the waveforms, which implies the event planes are parallel, and the small separation of most events compared with the source dimensions, which implies recurrent failure of parts of the same plane (Gaucher 1998). Tezuka & Niitsuma (2000) found this assumption held for multiplets in the Hijiori HDR reservoir in Japan. The diameter of the slip patches is considered a maximum value because it results from the assumption of radially symmetric rupture propagation at near the shear wave speed. The assumption of unilateral propagation or slower rupture propagation velocities would lead to smaller radii (Jones & Evans 2001). Most multiplets have superposed patches that suggest repeated rupture of the same asperity, perhaps a result in part of rising pore pressure (Baisch & Harjes 2003). However, there is invariably greater spread than can be ascribed to the relative location error of 1 m. That is, the events scatter about an area that is larger than the individual source dimensions, although not greatly so. That the events should be so tightly clustered suggests that they represent the progressive failure of a larger patch through stress transfer and/or rising pore pressure.

The structure of the lowermost part of the EL structure obtained from clustering analysis is shown in Fig. 22 (Phillips 2000). The relocated events define two planar structures that intersect without overlap. The planes, denoted 3 and 4 by Phillips, are high-angle features with strike/dips of 10°NE/80°W and 35°NW/80°E respectively that extend at least 80 m from their intersection (note 80 m was the radius of the event catchment sphere applied to the JHD cloud). The two planes formed sequentially: the NW-striking plane began to form 60 hr after the first event as part of the downward migration of events in the EL structure, whereas the NNE-striking plane did not begin to form until 112 hr (an animation showing the development of the two planes in 10 hr time steps is provided as supplementary material to this paper: file Soultz_93SEP01_LowerCluster.rm). The line of intersection of the two planes plunges in the same NNW direction as the EL structure but dips of 55° rather than 75°. For reasons explained in the next section, it seems probable that the NW-striking plane 4 is the downward continuation of the EL structure.

8 DISCUSSION

An interesting question is why the collapsed image suggested the EL structure was tubular rather than planar. This is largely a result of the ±50 m horizontal location error, which allows event locations to migrate towards the common centre of mass, which is a tube. Significantly smaller errors would be required to inhibit along-strike migration during collapsing and thus resolve the planar structure. Collapsing cannot resolve structures whose scale is smaller than the random error.
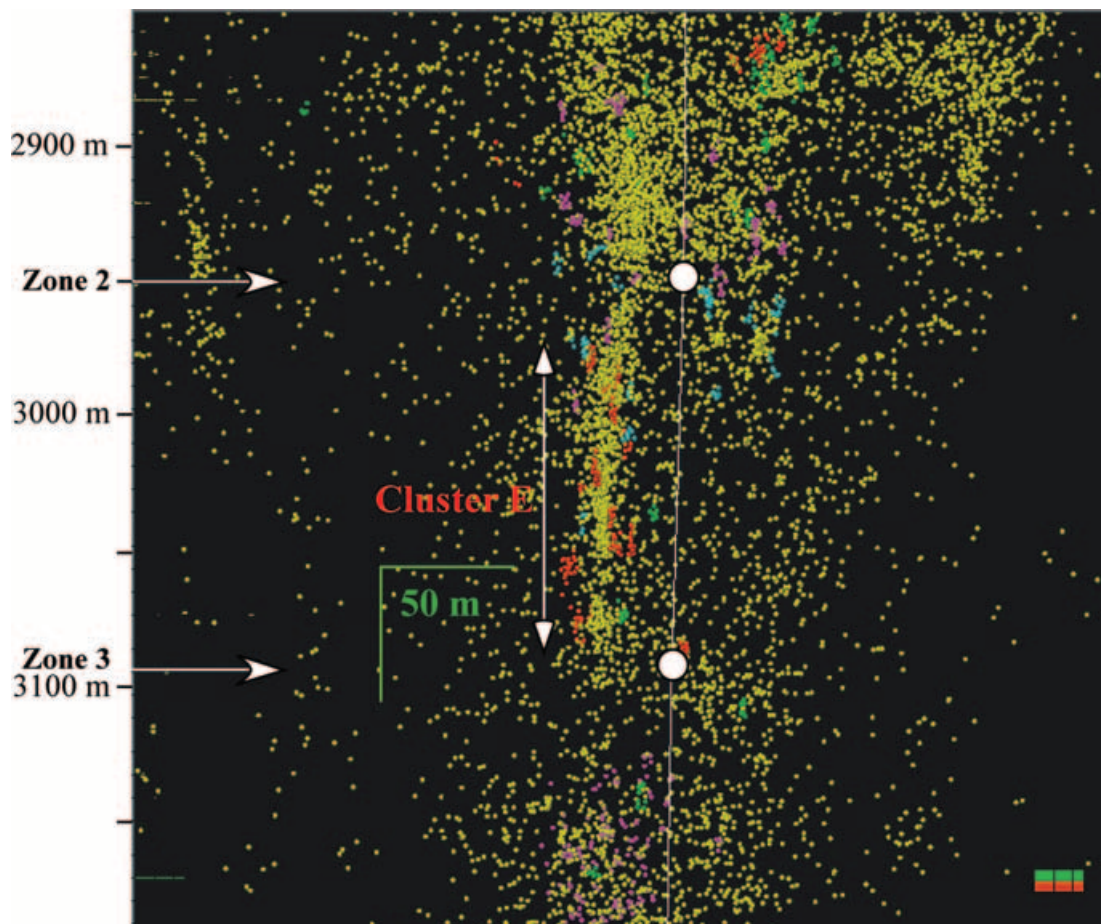
Figure 19. Multiplet groups after relocation with multiplet-clustering analysis viewed with the collapsed locations from 150°NE. Multiplets belonging the Multiplet-cluster E (MC-E) are shown in red. The absolute location of each cluster was chosen so that the centroid of the events it contains lays at the JHD location. The lowermost cloud of events form the lower cluster of Phillips (2000).

The planarity, scale and strike of MC-E and plane 4 of the lower cluster suggest they are the seismic expressions of the hydrothermally altered, cataclastic shear zones that have internal compositions similar to that shown in Fig. 5. The microseismic events appear to represent slip on the small-scale fractures within the structures. This explains why the multiplet planes scatter within 25° of parallel to the structure (Fig. 4d) and also why there is a marked upper limit of 8 m on the radii obtained from the source parameter analyses of all events (Jones & Evans 2001). This interpretation is also supported by borehole observations, which show that shearing and permeability creation/enhancement were limited to sections of hydrothermally-altered rock, which probably represent the intersection of the borehole with these structures (Evans *et al.* 2004).

Whether MC-E and plane 4 of the lower cluster are part of the same structure is uncertain: plane 4 dips at 80° to the east, whereas the plane of MC-E is almost vertical, and the seismicity becomes sparse in between the structures near 3130 m depth. Nevertheless, the continuous progression of microseismic events down the EL structure from one plane to the other, together with the hydraulic evidence for a continuous, low-impedance flow path extending from the top of the structure to the level of plane 4 suggests that if they are not parts of the same structure, they are at least hydraulically connected. The upward extent of the EL structure is difficult to trace owing to the dense seismicity that occurred during the later stages of the 93SEP01 stimulation. Upward extrapolation of the centre axis shown in Fig. 17(a) intersects the borehole in the vicinity of a

prominent, 7-m-long, hydrothermally altered zone lying 35 m above the casing shoe that produced hot fluid to the annulus during shut-ins and is almost certainly the expression of a 2.5-m-thick major shear structure (Genter *et al.* 1995). Substructures within this zone dip on average 68° to 244°NE and thus have a similar strike to the EL structure but a significantly shallower dip. Given the uncertainty in inferring the large-scale orientation of shear structures from local values, the relationship between the zone at 2810 m and EL structure is unclear.

The network of shear structures constitute the pathways through which fluid moves through the rock mass under natural conditions (Evans *et al.* 2004). However, their hydraulic characteristics are highly variable, as demonstrated by the range of permeabilities exhibited by those that intersect GPK1 (Sausse & Genter 2004). The primary hydraulic connection of the EL structure to the borehole appears to be the hydrothermally altered, zone 2 fracture complex at 2950 m, which was initially permeable and was the dominant flowing fracture in the hole at the early stages of the injection. Microseismicity moved down the structure from this point, although at a relatively slow rate of days (Figs 16 and 17b). Thus it seems likely that the structure itself was initially permeable, but not greatly so, at least in the large-scale connected sense. Following the stimulations, the evidence suggests that the structure hosted a relatively low impedance flow path (Fig. 11). Thus, it appears that the permeability of the structure was significantly enhanced as a consequence of the injection.
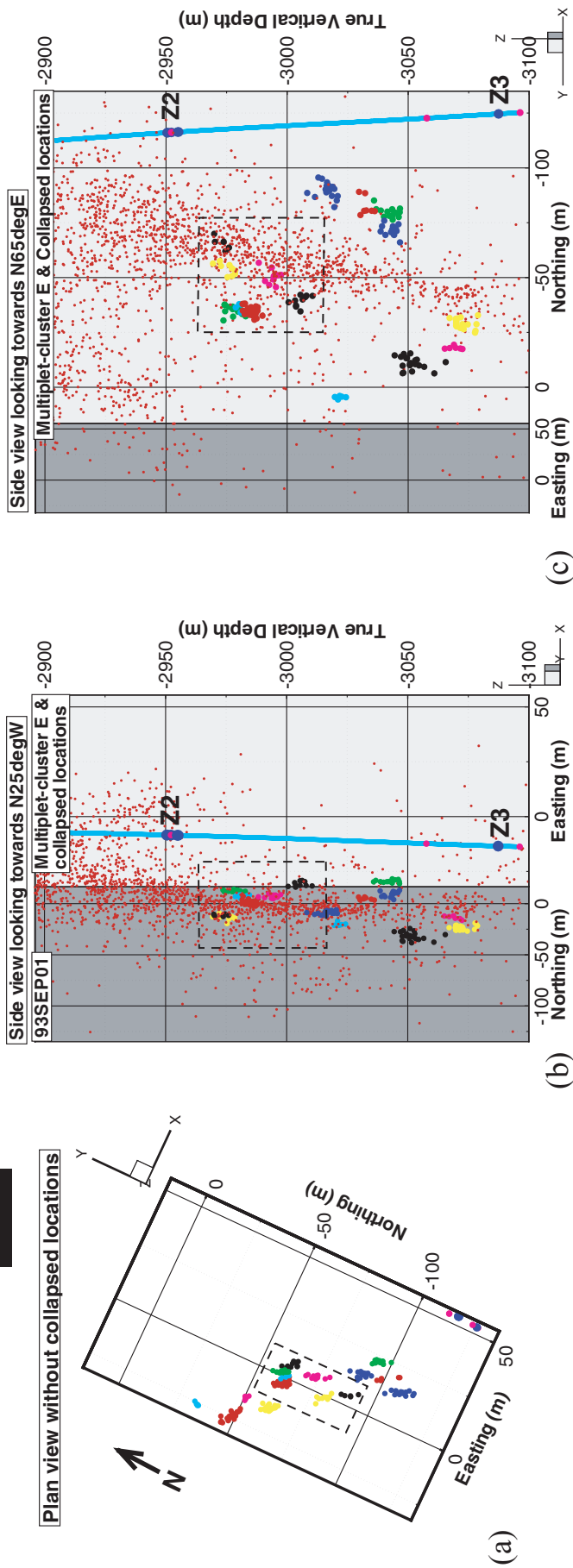
Figure 20. Views of multiplet-cluster E (MC-E), which lies within the EL structure just below the zone 2 fractures. The small groups of coloured dots denote the events comprising each multiplet, the different colours denoting different multiplets (with some colour duplication). The relative location error between events in each multiplet is less than 1 m and between multiplets it is less than 5 m. The collapsed cloud is shown in the two horizontal views but not the plan view. Both the events within the multiplets and the multiplets within the cluster define subvertical structures striking NNW.
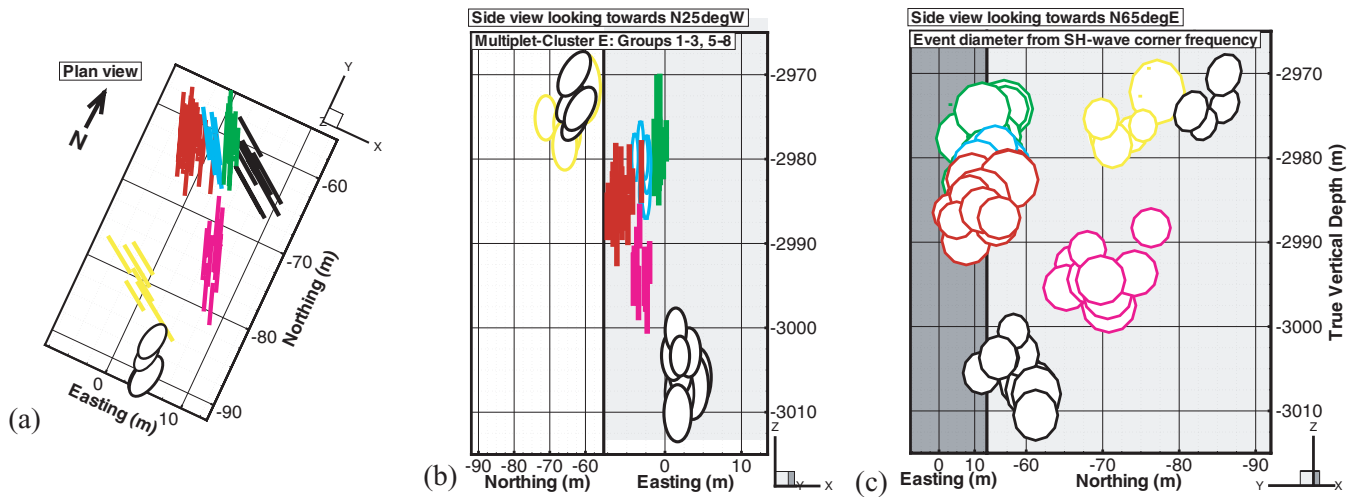
Figure 21. Close-up of the uppermost subcluster of multiplet-cluster E (MC-E) denoted by the box in Fig. 20 (same colour scheme). The events are shown as circular failure patches whose diameters are obtained from analysis of the corner frequency of *SH* waves and whose orientations are aligned with that of the multiplet plane to which they belong.

The majority of the stimulation occurred before the $181\,s^{-1}$ stage. At the start of this stage, the flow entering the rock mass at or below 2950 m was $6.2\,1\,s^{-1}$ and this increased by only a further $3.5\,1\,s^{-1}$ or 35 per cent in the remaining stages, the differential pressure driving the flow remaining essentially constant. The reduction in stimulation rate coincides with the termination of microseismic activity along the main structure, although it continues at the upper and lower extremes (e.g. the formation of plane 3 of the lower cluster). This is seen most clearly in the plots of seismic moment release history in successive 100-m-depth slices shown in Fig. 17(b). The continued
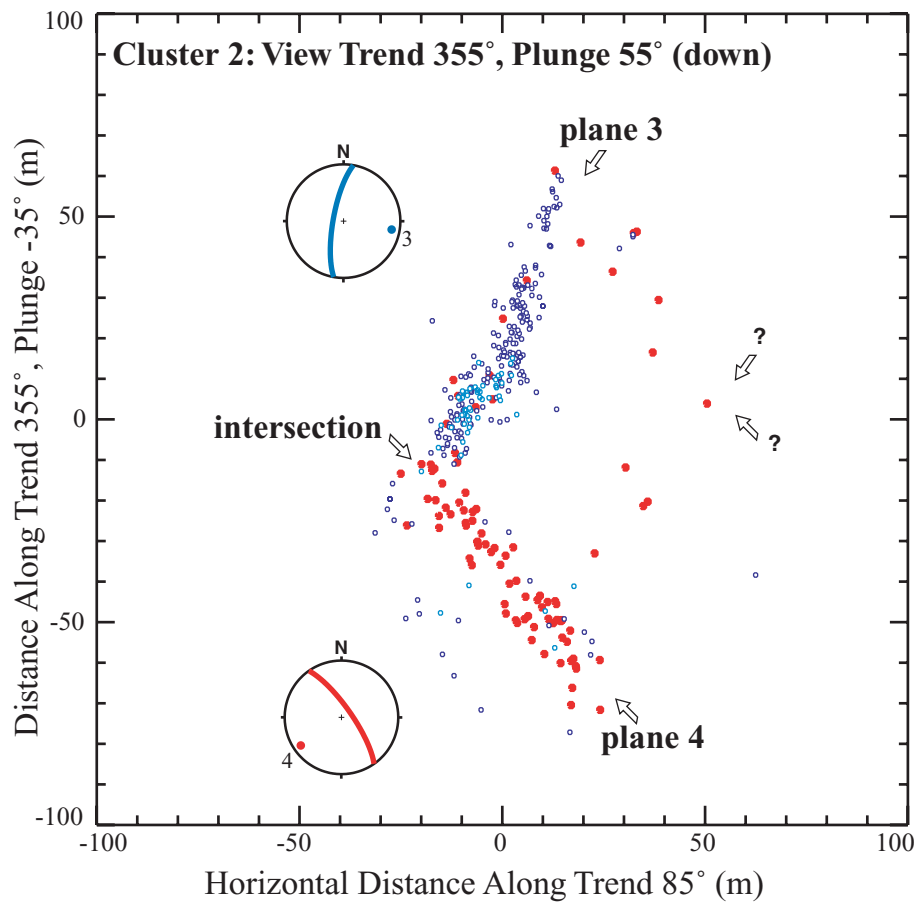

Figure 22. Events in the lower cluster of Phillips (2000; circled in Fig. 14b-3) after relocation by clustering analysis. The different colours denote events with similar waveforms and define two planes that intersect without overlapping. The view is along the intersection. The planes whose lower-hemisphere stereograms are shown strike NW and NNE. Whilst their intersection plunges in the same direction as the EL structure, it dips at $55°$ rather than $75°$.

increase in transmissivity after the 12 l s^{-1} stage probably reflects stimulation of the linking structures that connect the flow path(s) in the EL structure to the far field (Fig. 11). Whether these lie above or below the EL structure is unknown. Regarding the question of the fluid overpressure in the structure, a lower bound of 5 MPa is set by the inferred threshold for activation of seismicity and the upper bound of 9 MPa is set by the overpressure in the borehole. The low hydraulic impedance of the structure inherent in the conceptual model of Fig. 11 implies low pressure gradients and hence penetrative pressure whose magnitude would be limited by the entrance losses in the fracture zones near the borehole where the flow field becomes focussed. Modelling of hydraulic transients suggests these losses are not negligible (Kohl *et al.* 1998). Thus, the overpressure in the structure is constrained only to the range 5–9 MPa.

The available stress information favours shearing rather than jacking as the primary permeability creation/enhancement mechanism within the EL structure. This is illustrated in Fig. 6 where profiles of maximum well bore pressure prevailing along the hole during several stages of the injection are shown together with two possible profiles of S_{hmin}. Fractures that are approximately normal to S_{hmin}, which at Soultz is the minimum stress, can become fully jacked when their internal fluid pressure reaches the local value of S_{hmin}. For the reasons discussed earlier, the dotted S_{hmin} profile derived by excluding the hydrofracture data point at 3506 m is preferred. This profile predicts that full jacking conditions are restricted to the hole section above 2900 m for the 18 l s^{-1} and higher injection stages. For the depth range of the EL structure, well bore pressures are 1–2 MPa lower than required for full jacking. Consideration of entrance losses and poro-elastic stresses prevailing during injection increases this deficiency further (Evans 2004). Whilst fluid overpressures within the structure that are a few megapascals lower than S_{hmin} could still produce aperture increases during stimulation as a result of the normal compliance of fractures and perhaps produce full jacking at local stress perturbations, the primary stimulation mechanism is likely to be shearing. The geometry of the microseismic cloud supports this: above 2900 m the structures in the cloud strike N–S, suggesting stress control through jacking, whereas below 2900 m the structures strike NNW, suggesting geological-structure control through shearing (Cornet & Jones 1994; Fabriol *et al.* 1994). Such structures would be optimally oriented for shear failure in the prevailing stress field. Thus, mechanisms related to shearing offer a more viable explanation of permeability enhancement along the EL structure, although jacking mechanisms such as proposed by Jung & Weidler (2000) may be relevant for the shallowest levels of the structure near 2950 m. Observations at the borehole wall support this. Almost all major flowing fractures suffered measurable dislocation of millimetres to centimetres, mostly in shear, and the majority of newly permeable fractures also showed evidence of damage, most likely through shear failure (Evans *et al.* 2004).

Whilst it is generally recognized that shearing leads to dilation and permeability increases, this in itself does not explain why the stimulation apparently progressed downwards and was restricted to a relatively narrow zone. Pine & Batchelor (1984) describe similar observations of microseismicity at the UK HDR test site in Cornwall and ascribe the downward propagation to the vertical gradient of *in situ* stress. Given the uncertainty in the profile of S_{Hmax} at Soultz, stress control of the downward growth cannot be ruled out, although the marked upward growth seen after the 12 l s^{-1} stage suggests otherwise. An alternative or complementary explanation is that the downward migration reflects the effects of along-strike jogs in the surface undergoing shear. This mechanism, illustrated in Fig. 23, was originally proposed by Hill (1977) to explain earthquake swarms, and was further developed by Sibson (1996) to explain mineral veins and Tezuka & Niitsuma (2000) to explain stimulation of
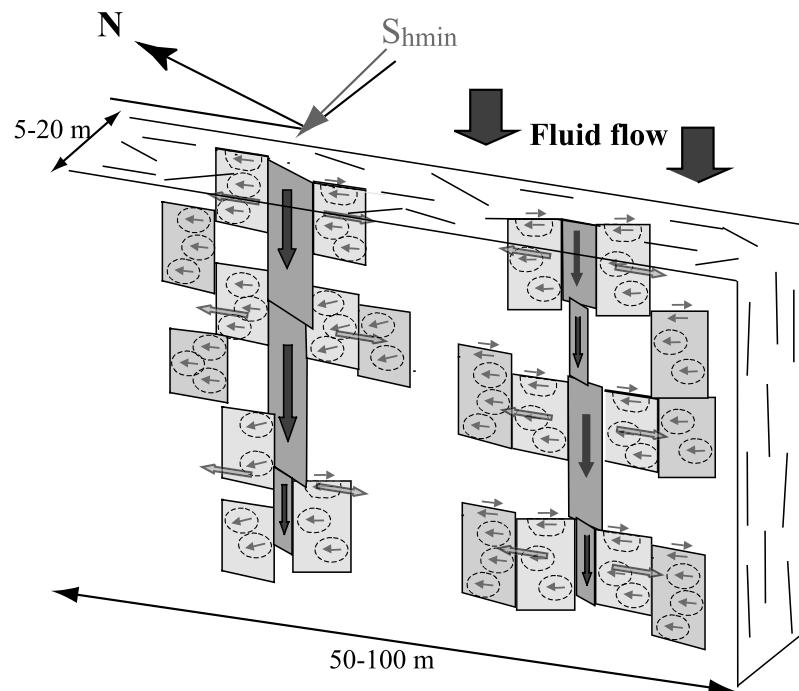

Figure 23. Illustration showing a simplified, 2-D scheme of slip within a major shear structure that strikes 25°NW. The network denotes small-scale fractures internal to the structure. Strike-slip displacement occurs on vertical fractures that strike parallel to the structure and are optimally oriented for failure. Extensive, coherent slip within the structure will involve the development of an irregular slip surface with jogs reflecting linkage. At right-stepping jogs the dislocation will have a large opening-mode component under right-lateral shear, resulting in the formation of a vertical, open tube. The events in the multiplets occur on the fracture elements.

permeability at the Hijiori HDR site. It has also been identified in laboratory experiments (Yeo *et al.* 1998). The effect of through-going, right-lateral shear on a surface that has a right-stepping offset running downwards is to open a tube along the offset. This pull-apart mechanism is geometrically similar to the stimulation mechanism proposed by Jung & Weidler (2000) where the tube is a hydrofracture confined between two surfaces that shear in response to pressurization from the hydrofracture (Keer & Chen 1981). However, in Hill's concept, the tube opens as a result of slip on the shearing fractures rather than the other way round. It is known that the surface roughness of faults tends to be greatest in the direction normal to the slip vector (i.e. normal to the slickenside direction; Lee & Bruhn 1996). In the present context, the anisotropic roughness of normal fault surfaces activated in strike-slip mode would best promote the development of vertical tubes that could account for the preferred downward migration of fluid pressure (Brown & Bruhn 1996). Evidence that the events defining plane 4 predominantly involved right-lateral slip was given by Phillips (2000) who determined focal mechanisms using *P*-wave polarities with the constraint that slip lies in the seismically defined plane, although events from the cloud as a whole indicate predominant normal faulting (Helm 1996; Gaucher *et al.* 1998).

An estimate of the amount of seismic slip developed in the structure during the injection can be obtained from the cumulative seismic moment, *Mo*, released in each of the 100-m-depth slices along the EL structure shown in Fig. 17(b). For most slices below 2900 m, this is of the order of 1×10^{11} N m. Assuming this moment is released uniformly over a zone of along-strike length 100 m, then the mean slip, δ, can be calculated from the relation,

$$\delta = Mo/(\mu \cdot A), \tag{1}$$

where A is the area given by 1×10^4 m^2 for each section and μ is the static shear modulus. Using a value for shear modulus of 3×10^{10} Pa derived from sonic and density logs run in the well and three-point bending tests (Rummel 1989) yields an estimate for average slip of 0.3 mm. Whilst this is small in comparison with the millimetres-to-centimetres of slip on the major flowing fractures at the borehole (Poitrenaud 1994; Evans 2001a,b), it is nevertheless sufficient to produce significant changes in flow, as a simple scoping calculation based on the cubic law shows. Consider the fault as a smooth, parallel plate of along-strike breadth, b (=100 m), downdip length, l (500 m) and hydraulic aperture, a_h. If a pressure gradient of $\Delta P/dl$ exists in the downdip direction, then the net flow downdip is given by (e.g. de Marsily 1986 p. 55)

$$Q = \left(a_h^3 \, b \Delta P/dl\right)/(12n), \tag{2}$$

where $n =$ dynamic viscosity (=$2 \times 10^{-4}-$ Pa s for water at 150°C). If the mechanical dilation, a_m, resulting from the slip, δ, of 0.3 mm is given by $a_m = \delta \tan\theta$, where θ is the dilation angle (=30°), then the change in plate separation is 0.17 mm. Suppose further that the flow is driven by a 9-MPa pressure difference at either end of the 500-m-long structure so that the pressure gradient is 1.8×10^{-4} Pa m. If the initial permeability/aperture is taken as zero, the change in flow through the structure as a result of 0.3 mm of slip is 3.7 l s^{-1} (eq. 2). Larger changes in flow result from assuming non-zero initial aperture. For example, if the initial aperture is 0.05 mm, which would admit an (unstimulated) steady-state flow of 0.1 l s^{-1} under the given pressure gradient, then an increase of 0.17 mm would produce a flow increase of 8 l s^{-1}. Whilst it is encouraging that these flow rate changes are of the correct order of magnitude, the agreement should not be taken as a validation of the model. For if the hydraulic conceptual model of Fig. 11 is correct, then

pressure gradients within the structure are substantially less than the value assumed and the predicted flow rate changes would be correspondingly less. We consider it equally, if not more probable that the moment release is concentrated on stimulating hydraulic barriers in a fault zone that already has significant, but vertically discontinuous permeability. The multiplets in Fig. 21, which largely reflect repeated slip on and about asperities are consistent with this. Another possibility is that a large fraction of the net slip on the structure occurred aseismically. There is considerable evidence for aseismic slip within the reservoir, particularly above 2950 m (Cornet *et al.* 1997; Evans 1998), although the data for the EL structure do not demand it.

Finally, there is the question of the implications of the results for the development of the HDR reservoir. The collapsed cloud of microseismicity induced by 1993 stimulations shows many examples of propagating tubular or planar structures, many of which are subvertical and oriented towards NNW (Cornet & Jones 1994; Rowe *et al.* 2002). Presumably these reflect the advance of pressure along hydrothermally altered shear structures that have a preferred strike of NNW–SSE and it is likely that their permeability was also enhanced as a consequence, although not necessarily through the same mechanism. The results thus suggest that stimulation in the reservoir is largely confined to the flow paths defined within the interior of these fracture zones. As such, the spreading of the flow field would be much less than expected for radial flow through a porous medium, an implication that is consistent with the indications that turbulent-like flow extends considerable distances from the well bore (Kohl *et al.* 1998). The surface area swept by the flow, which is an important factor for the long-term thermal performance of the reservoir under circulation, would thus depend critically on the intact block size. Genter & Castaing (1997) suggest this is of the order of 100 m.

9 CONCLUSION

The 1993 September stimulation of the 3–3.5 km depth reservoir at the Soultz site is well suited to investigating porosity/permeability creation processes in low-permeability granite because the rock mass was relatively undisturbed and the associated data set is exceptionally complete. The injection generated a subvertical cloud of microseismicity approximately 0.5 km wide, 1.2 km long, 1.5 km high and oriented 25°NW. Collapsing applied to the JHD locations revealed the cloud to be composed largely of discrete tubes and planes that propagate coherently. One such structure extended some 350 m downwards from the vicinity of a flowing fracture zone in the borehole at 2950 m and appeared to contain a relatively high-permeability flow path that linked two flow zones in the borehole 200 m apart. This structure was subjected to a detailed interdisciplinary investigation to establish its geological nature and the processes that accounted for its apparent hydrological significance.

High location precision images of the microseismicity show the structure to be a narrow, vertical zone of width 5–20 m, which strikes 25°NW. The microseismic events were generated by slip on subvertical planes whose azimuths scatter $\pm$ 22° from parallel with the parent structure. The radius of the slip patches of individual events are less than 8 m. These observations identify the structure as a member of a family of subvertical, hydrothermally-altered cataclastic shear zones that are the primary structures present in the basement. The shear structures have widths up to several tens of metres and include numerous limited-scale fractures, which generally show slickensides. Slip on these fractures generates the microseismicity. These structures tend to strike 20°NW and are close to optimally oriented for strike-slip shear failure in the prevailing stress field.

The slow advance of microseismicity down the structure over a period of days in the early stages of the injection suggests the initial connected permeability was not high. However, following the injections, the structure contains a propped, high-permeability flow path. The enhancement of permeability occurred early in the injections when microseismic energy release rate was greatest. Available stress information suggests that the mechanism underpinning this permeability increase involved shear. The slip implied by the cumulative seismic moment release is at least 0.3 mm and more if the seismic slip is focussed on barriers. Significant changes in flow could result from such displacements. The preferred mechanism of permeability enhancement involves the reactivation in strike-slip of structures with a roughness anisotropy characteristic of normal faults. This would result in the opening of vertical tubes at jogs in the fault in the manner proposed by Hill (1977) and can thus explain the downward migration of microseismicity.

Borehole observations show that shearing and permeability creation/enhancement are confined to zones of hydrothermally altered rock associated with the cataclastic, shear structures. Thus, it is likely that most microseismicity represents fluid penetration along these structures, which contain the flow paths through which fluid moves through the rock mass under natural conditions. Consequently, permeability enhancement will largely be confined to the structures with little enhancement occurring in the blocks they bound.

ACKNOWLEDGMENTS

SUPPLEMENTARY MATERIAL

Three animations showing the development of microseismicity for the full cloud, the EL structure and the lower cluster are available for download from http://www.blackwellpublishing.com/products/journals/suppmat/GJI/GJI2474/GJI2474sm.htm.

REFERENCES

Abé, H., Niitsuma, H. & Baria, R., 1999. Preface to the Hot Dry Rock/Hot Wet Rock Academic Review, *Geothermics,* **28,** 451–679.

Audigane, P., Royer, J.-J. & Kaieda, H., 2002. Permeability characterization of the Soultz and Ogachi large-scale reservoir using induced microseismicity, *Geophysics,* **67,** 204–211.

Baisch, S. & Harjes, H.-P., 2003. A model for fluid-injection-induced seismicity at the KTB, Germany, *Geophys. J. Int.,* **152,** 160–170.

Baisch, S., Bohnhoff, M., Ceranna, L., Tu, Y. & Harjes, H.-P., 2002. Probing the crust to 9 km depth: Fluid-injection experiments and induced seismicity at the KTB Superdeep Drilling Hole, Germany, *Bull. seism. Soc. Am.,* **92,** 2369–2380.

Baumgärtner, J. & Rummel, F., 1989. Experience with 'fracture pressurization tests' as a stress measuring technique in a jointed rock mass, *Int. J. Rock Mech. Min. Sci. & Geomech. Abstr.,* **26,** 661–671.

Baumgärtner, J., Jung, R., Gérard, A., Baria, R. & Garnish, J., 1996. The European Hot Dry Rock Project at Soultz sous Forêts: Stimulation of the second deep well and the first circulation experiments. In: *21st Workshop on Geothermal Reservoir Engineering, Stanford University, Stanford, California, January 22–24* pp. 267–274, Stanford University, Stanford, CA, USA.

Baumgärtner, J., Gérard, A., Baria, R., Jung, R., Tran-Viet, T., Gandy, T., Aquilina, L. & Garnish, J., 1998. Circulating the HDR reservoir at Soultz: Maintaining production and injection flow in complete balance. In: *23rd Workshop on Geothermal Reservoir Engineering, Stanford University, Stanford, California, 26–28th January* pp. 11–20, Stanford University, Stanford, CA, USA.

Bérard, T. & Cornet, F., 2003. Evidence of thermally induced borehole elongation: a case study at Soultz, France, *Int. J. Rock Mech. Min. Sci.,* **40,** 1121–1140.

Brown, S.R. & Bruhn, R., 1996. Formation of voids and veins during faulting, *J. Struct. Geol.,* **18,** 657–671.

Brudy, M. & Zoback, M. D., 1999. Drilling-induced tensile wall-fractures: implications for determination of in-situ stress orientation and magnitude, *Int. J. Rock Mech. Min. Sci.,* **36,** 191–215.

Cash, D.J., Homuth, E.F., Keppler, H., Pearson, C. & Sasaki, S., 1983. Fault plane solutions for microearthquakes induced at the Fenton Hill Hot Dry Rock geothermal site: Implications for the state of stress near a Quaternary volcanic centre, *Geophys. Res. Lett.,* **10,** 1141–1144.

Cornet, F.H. & Jones, R.H., 1994. Field evidence on the orientation of forced water flow with respect to the regional principal stress directions. In: eds Nelson, P.P. & Laubach, S.E., *1st North American Rock Mechanics Symposium,* pp. 61–69, Balkema, Austin, TX, USA.

Cornet, F.H. & Julian, P., 1989. Stress determination from hydraulic test data and focal mechanisms of induced earthquakes, *Int. J. Rock Mech. Min. Sci. & Geomech. Abstr.,* **26,** 235–248.

Cornet, F.H. & Scotti, O., 1993. Analysis of induced seismicity for fault zone identification, *Int. J. Rock Mech. Min. Sci. & Geomech. Abst.,* **30,** 789–795.

Cornet, F.H., Helm, J., Poitrenaud, H. & Etchecopar, A., 1997. Seismic and aseismic slip induced by large fluid injections, *Pure appl. Geophys.,* **150,** 563–583.

Darnet, M., 2000. *Caractérisation microseismique d'un massif hydrauliquement stimulé* Mémoire de DEA, Université Louis Pasteur, Strasbourg, France.

Dezayes, C.T., Villemin, T., Genter, A., Traineau, H. & Angelier, J., 1995. Analysis of fractures in boreholes of Hot Dry Rock project at Soultz-sous-Forêts (Rhine Graben, France), *J. Sci. Drill.,* **5,** 31–41.

Dyer, B.C., Baria, R. & Asanuma, H., 2001. An investigation of the resolution of the Soultz 2000 seismic locations, in, *Final report to New Energy Development Organisation (NEDO), Japan for the Project 'Universal Understanding and Design of Engineered Geothermal Systems',* Semore Seismic, Falmouth, UK.

Evans, K.F., 1998. Does significant aseismic slip occur on fractures in HDR systems under stimulation conditions? In: ed., *Pre-conference proc. of 4th Int. Hot Dry Rock Forum, SOCOMINE, Kutzenhausen, France, 28–30 September.*

Evans, K.F., 2000. The effect of the 1993 stimulations of well GPK1 at Soultz on the surrounding rock mass: Evidence for the existence of a connected network of permeable fractures. In: eds Iglesias, E. *et al.*, *World Geothermal Congress, Morioka, Japan, May 28th–June 10th,* pp. 3695–3700, International Geothermal Association, Reykjavik, Iceland.

Evans, K.F., 2001a. Quantitative assessment of slip occurring on fractures during the 1993 stimulation of GPK1 at Soultz-sous-Forêts, France from BHTV travel time data, in, *Final report to New Energy Development Organisation (NEDO), Japan for the Project 'Universal Understanding and Design of Engineered Geothermal Systems'.*

Evans, K.F., 2001b. Determining the effect of stimulation injections on the rock mass around the well GPK1 from borehole data: analysis of the 1993 injections, in, *Final report to the Swiss Department of Education and*

Science (BBW) under contract BBW 98.0008–1, Swiss Federal Institute of Technology, 29–74, ETH-Hoenggebey, Zurich, Switzerland.

Evans, K.F., 2004. Permeability creation and damage due to massive fluid injections into granite at 3.5 km at Soultz: Part 2 - Stress and fracture strength, *J. geophys. Res.,* submitted.

Evans, K.F., Kohl, T., Hopkirk, R.J. & Rybach, L., 1992. Modelling of energy production from Hot Dry Rock systems, in *Final Report to Swiss National Energy Research Fund (NEFF) under contract NEFF 359,* Swiss Federal Institute of Technology/Polydynamics, 316, ETH-Hoenggebey, Zurich, Switzerland.

Evans, K.F., Kohl, T., Hopkirk, R.J. & Rybach, L., 1996. Studies of the nature of non-linear impedance to flow within the fractured granitic reservoir at the European Hot Dry Rock Project site at Soultz-sous-Forêts, France, in, *Final report to the Swiss Department of Education and Science (BBW) under contract BBW 93.0010,* Swiss Federal Institute of Technology/Polydynamics Engineering, 144, ETH-Hoenggebey, Zurich, Switzerland.

Evans, K.F., Genter, A. & Sausse, J., 2004. Permeability creation and damage due to massive fluid injections into granite at 3.5 km at Soultz: Part 1 - Borehole observations, *J. geophys. Res.,* submitted.

Fabriol, H., Beauce, A., Genter, A. & Jones, R., 1994. Induced seismicity and its relation with natural fractures: the HDR example of Soultz (France), *Geothermal Resources Council Transactions,* **18**, 423–430.

Fehler, M., Jupe, A. & Asanuma, H., 2001. More Than Cloud: New techniques for characterising reservoir structure using induced seismicity, *The Leading Edge,* **20**(3), 324–328.

Fréchet, J., Martel, L., Nikolla, L. & Poupinet, G., 1989. Application of the cross-spectral moving-window technique (CSMWT) to the seismic monitoring of forced fluid migration in a rock mass, *Int. J. Rock Mech. Min. Sci. & Geomech. Abstr.,* **26**, 221–233.

Frohlich, C., 1979. An efficient method for joint hypocentral determination for large groups of earthquakes, *Comput. Geosci.,* **5**, 387–389.

Gaucher, E., 1998. Comportement hydromécanique d'un massif fracturé: apport de la microseismicité induite, *PhD thesis*, Université de Paris 7, Paris, France.

Gaucher, E., Cornet, F. H. & Bernard, P., 1998. Induced seismicity analysis for structure identification and stress fields determination, SPE Paper 47324. In: *Eurock 98, Trondheim, Norway, 8–10 July 1998,* Society of Petroleum Engineers, **1**, 545–554, Richardson, TX, USA.

Genter, A., 1989. Géothermie Roches Chaudes Sèches: le granite de Soultz-sous-Forêts, (Bas-Rhin, France), *PhD thesis*, Université d'Orléans, Orleans, France.

Genter, A. & Castaing, C., 1997. Effets d'échelle dans la fracturation des granites (Scale effects in the fracturing of granite), *C.R. Acad. Sci. Paris, Science de la terre et des planètes,* **325**, 439–445.

Genter, A. & Traineau, H., 1992. Borehole EPS-1, Alsace, France: preliminary geological results from granite core analyses from Hot Dry Rock research, *Scientific Drilling,* **3**, 205–214.

Genter, A. & Traineau, H., 1996. Analysis of microscopic fractures in granite in the HDR geothermal well EPS-1, Soultz-sous-Forêts, France, *J. Volc. Geotherm. Res.,* **72**, 121–141.

Genter, A., Traineau, H., Dezayes, C., Elsass, P., Ledesert, B., Meunier, A. & Villemin, T., 1995. Fracture analysis and reservoir characterization of the granitic basement in the HDR Soultz project (France)., *Geotherm. Sci. & Tech.,* **4**, 189–214.

Genter, A., Castaing, C., Dezayes, C., Tenzer, H., Traineau, H. & Villemin, T., 1997. Comparative analysis of direct (core) and indirect (borehole imaging tools) collection of fracture data in the Hot Dry Rock Soultz reservoir (France), *J. geophys. Res.,* **102**, 15 419–15 431.

Genter, A., Dezayes, C., Gentier, S., Ledesert, B. & Sausse, J., 1998. Conceptual fracture model at Soultz based on geological data. In: *Geologisches Jahrbuch, Sondeheft: Reihe E (Geophysik), Heft SE1 (International Hot Dry Rock Forum, Strasbourg, France, September 28–30th 1998)*, pp. 93–102 eds Bario, R. **et al.** Schweizerbart'sche verlogbuchhandlung, Stuttgart, Germany.

Genter, A., Traineau, H., Ledésert, B., Bourgine, B. & Gentier, S., 2000. Over 10 years of geological investigations within the HDR Soultz Project, France. In: *World Geothermal Congress, Morioka, Japan, May 28th–June 10th,* eds Iglesias, E. *et al.*, pp. 3707– 3712, International Geothermal Association, Reykjavik, Iceland.

Helm, J.A., 1996. The natural seismic hazard and induced seismicity of the European HDR (Hot Dry Rock) geothermal energy project at Soultz-sous-Forêts, France, *PhD thesis*, Université Louis-Pasteur, Strasbourg, France.

Hettkamp, T., Baumgärtner, J., Baria, R., Gerard, A., Gandy, T., Michelet, S. & Teza, D., 2004. Electricity production from Hot Rocks. In: *29th Workshop on Geothermal Reservoir Engineering, Stanford University, Stanford, California, Jan. 26–28,* pp. 184– 193, Stanford University, Stanford, CA, USA.

Hill, D.P., 1977. A model for earthquake swarms, *J. geophys. Res.,* **82**, 1347–1352.

Ito, T., Evans, K., Kawai, K. & Hayashi, K., 1999. Hydraulic fracture re-opening pressure and the estimation of maximum horizontal stress, *Int. J. Rock Mech. Min. Sci. & Geomech. Abstr.,* **36**, 811–826.

Jones, R.H. & Evans, K.F., 2001. Improved source parameter estimates from microseismic events occurring during the 1993 injections of GPK1 at Soultz-sous-Forêts, in, *Final report to New Energy Development Organisation (NEDO), Japan for the Project 'Universal Understanding and Design of Engineered Geothermal Systems.*

Jones, R.H. & Stewart, R.C., 1997. A method for determining significant structures in a cloud of earthquakes, *J. geophys. Res.,* **102**, 8245–8254.

Jones, R.H., Beauce, A., Jupe, A., Fabriol, H. & Dyer, B.C., 1995. Imaging induced seismicity during the 1993 injection test at Soultz-sous-Forêts, France, in *World Geothermal Congress, Florence, Italy, 18–31st May,* eds Barbier, E., *et al.*, pp. 2665– 2669, International Geothermal Association, Reyklovic, Iceland.

Jost, M.L., Büsselberg, T., Jost, Ö. & Harjes, H.-P., 1998. Source parameters of injection-induced microearthquakes at 9 km depth at the KTB deep drilling site, Germany, *Bull. seism. Soc. Am.,* **88**, 815–832.

Jung, R. & Weidler, R., 2000. A conceptual model for the stimulation process of the HDR-system at Soultz, *Geothermal Resources Council Transactions,* **24**, 143–147.

Jung, R., Willis-Richards, J., Nicholls, J., Bertozzi, A. & Heinemann, B., 1995. Evaluation of hydraulic tests at Soultz-sous-Forets, European Hot Dry Rock site. In: eds Barbier, E. *et al.*, *World Geothermal Congress, Florence, Italy, 18–31st May,* pp. 2671– 2676, International Geothermal Association, Reyklovic, Iceland.

Jupe, A.J., Willis-Richards, J. & Nichols, J.D., 1993. Review of HDR Projects, in *Report to UK Department of Trade and Industry, ETSU-G-164-p1, HMSO.*

Keer, L.M. & Chen, S.H., 1981. The intersection of a pressurized crack with a joint, *J. geophys. Res.,* **86**, 1032–1038.

Klee, G. & Rummel, F., 1993. Hydrofrac stress data for the European HDR research project test site Soultz-sous-Forêts, *Int. J. Rock Mech. Min. Sci. & Geomech. Abst.,* **30**, 973–976.

Kohl, T., Evans, K.F., Hopkirk, R.J., Jung, R. & Rybach, L., 1997. Observation and simulation of non-Darcian flow transients in fractured rock, *Wat. Resourc. Res.,* **33**, 407–418.

Kohl, T., Evans, K.F. & Rybach, L.R., 1998. Identifying the hydraulic regime at the Soultz Hot Dry Rock test site: constraints on reservoir geometry. In: ed. *Pre-conference proc. of the 4th Int. Hot Dry Rock Forum, SOCOMINE, Kutzenhausen, France, 28–30 September.*

Larroque, J.M. & Laurent, P., 1988. Evolution of the stress field pattern in the south of the Rhine Graben from Eocene to the present, *Tectonophysics,* **148**, 41–58.

Lee, J.-J. & Bruhn, R., 1996. Structural anisotropy of normal fault surfaces, *J. Struct. Geol.,* **18**, 1043–1059.

Maillot, B., Nielsen, S. & Main, I., 1999. Numerical simulations of seismicity due to fluid injection in a brittle poroelastic medium, *Geophys. J. Int.,* **139**, 263–272.

de Marsily, G., 1986. *Quantitative Hydrogeology,* Academic Press, London, UK, p. 440.

Moriya, H., Nakazato, K., Evans, K.F., Niitsuma, H., Jones, R. H. & Baria, R., 2001. Evaluation of the Soultz HDR system by precise mapping techniques of induced microseismic events, *Trans. Geothermal Resources Council,* **25**, 187–190.

Moriya, H., Nakazato, K., Niitsuma, H. & Baria, R., 2002. Detailed fracture system of the Soultz-sous-Forêts HDR field evaluated using microseismic multiplet analysis, *Pure appl. Geophys.,* **159**, 517–541.

Moriya, H., Niitsuma, H. & Baria, R., 2003. Multiplet-clustering analysis for estimation of fine detail structures in seismic clouds at Soultz field, France, *Bull. seism. Soc. Am.,* **93**, 1606–1620.

Niitsuma, H. *et al.*, 1999. Current status of seismic and borehole measurements for HDR/HWR development, *Geothermics,* **29**, 475–490.

Phillips, W.S., 2000. Precise microearthquake locations and fluid flow in the geothermal reservoir at Soultz-sous-Forêts, France, *Bull. seism. Soc. Am.,* **90**, 212–228.

Phillips, S., House, L.S. & Fehler, M.C., 1997. Detailed joint structure in a geothermal reservoir from studies of induced microseismic clusters, *J. geophys. Res.,* **102**, 11 745–11 763.

Pine, R.J. & Batchelor, A.S., 1984. Downward migration of shearing in jointed rock during hydraulic injections, *Int. J. Rock Mech., Min. Sci. & Geomech. Abstr.,* **21**, 249–263.

Plenefisch, T. & Bonjer, K.-P., 1997. The stress field in the Rhine Graben area inferred from earthquake focal mechanisms and estimation of frictional parameters, *Tectonophysics,* **275**, 71–97.

Poitrenaud, H., 1994. Application des mesures par 'ultrasonic borehole imager' à la détermination de glissements sur fractures preexistants, rapport de DESS, *MSc thesis*, Institut de physique du globe, Paris, France (in French).

Poupinet, G., Ellsworth, W.L. & Fréchet, J., 1984. Monitoring velocity variations in crust using earthquake doublets: An application to the Calaveras fault, California, *J. Geophys, Res.,* **89**, 5719–5731.

Roff, A., Phillips, W.S. & Brown, D.W., 1996. Joint structures determined by clustering microearthquakes using waveform amplitude ratios, *Int. J. Rock Mech. Min. Sci. and Geomech. Abstr.,* **33**, 627–639.

Rowe, C.A., Aster, R.C., Phillips, W.S., Jones, R.H., Borchers, B. & Fehler, M.C., 2002. Automated high-precision repicking to improve delineation of microseismic structures at the Soultz geothermal reservoir, *Pure appl. Geophys.,* **159**, 563–596.

Rummel, F., 1989. *Fracture mechanics properties of granite cores from GPK1,* Report Number 7, Ruhr University, Bochum, Germany.

Rummel, F., 1991. Physical properties of the rock in the granitic section of borehole GPK1, Soultz-sous-Forêts, *Geotherm. Sci. and Tech.,* **3**, 199–216.

Rummel, F. & Klee, G., 1995. State of stress at the European candidate sites Urach and Soultz. In: eds Barbier, E. *et al.*, *World Geothermal Congress, Florence, Italy, 18–31st May,* pp. 2639–2642, International Geothermal Association, Reyklovic, Iceland.

Rutqvist, J., Tsang, C.F. & Stephansson, O., 2000. Uncertainty in the maximum principal stress estimated from hydraulic fracturing measurements due to the presence of the induced fracture, *Int. J. Rock Mech. Min. Sci.,* **37**, 107–120.

Sausse, J., 2000. Traitement graphique des données de forage: caractérisation des relations fracturation - altérations. Application au granite de Soultz-sous-Forêts (Bas-Rhin, France), *Comptes rendus de l'Académie des sciences. Série II. Sciences de la terre et des planètes.,* **330**, 185–192.

Sausse, J. & Genter, A., 2004. Two types of fracture permeability in granite, *Proc. Geol. Soc. Lond.,* Special Publication 796, Petrophysicol Properties of Crystolline Rocks, in press.

Shapiro, S.A., Audigane, P. & Royer, J.-J., 1999. Large-scale in-situ permeability tensor of rocks from induced seismicity, *Geophys. J. Int.,* **137**, 207–213.

Sibson, R., 1996. Structural permeability of fluid-driven fault-fracture meshes, *J. Struct. Geol.,* **18**, 1031–1042.

Tezuka, K. & Niitsuma, H., 2000. Stress estimated using microseismic clusters and its relationship to the fracture system of the Hijiori Hot Dry Rock reservoir, *Engineering Geology,* **56**, 47–62.

Thurber, C.H. & Rabinowitz, N., 2000. Advances in seismic event location, in, *Modern approaches in geophysics,* Kluwer Academic Publishers, Dordrecht, the Netherlands, p. 266.

Wallroth, T., Jupe, A.J. & Jones, R.H., 1996. Characterisation of a fractured reservoir using microearthquakes induced by hydraulic injections, *Mar. and Petrol. Geol.,* **13**, 447–455.

Weidler, R., Gerard, A., Baria, R., Baumgärtner, J. & Jung, R., 2002. Hydraulic and micro-seismic results of a massive stimulation test at 5 km depth at the European Hot-Dry-Rock test site, Soultz, France. In: *27th Workshop on Geothermal Reservoir Engineering, Stanford University, Stanford, California, Jan. 28–30*, pp. 241–251, Stanford University, Stanford, CA, USA.

Yeo, I.W., De Frietas, M.H. & Zimmerman, R.W., 1998. Effect of shear displacement on the aperture and permeability of a rock fracture, *Int. J. Rock. Mech. Min. Sci.,* **35**, 1051–1070.